Transiting exoplanets from the CoRoT space mission XXIX. The hot Jupiters CoRoT-30 b and CoRoT-31 b

P. Bordé, R. Díaz, O. Creevey, C. Damiani, H. Deeg, P. Klagyivik, G. Wuchterl, D. Gandolfi, M. Fridlund, F. Bouchy, et al.

A&A 635, A122 (2020)
https://doi.org/10.1051/0004-6361/201732393

Astronomy & Astrophysics

Transiting exoplanets from the CoRoT space mission

XXIX. The hot Jupiters CoRoT-30 b and CoRoT-31 b*

P. Bordé[1], R. F. Díaz[2,3,4], O. Creevey[5,6], C. Damiani[6,7], H. Deeg[10,11], P. Klagyivik[10,11], G. Wuchterl[29], D. Gandolfi[8,9], M. Fridlund[12,13,14], F. Bouchy[2,16], S. Aigrain[15], R. Alonso[10,11], J.-M. Almenara[2,16], A. Baglin[17], S. C. C. Barros[16,18], A. S. Bonomo[19], J. Cabrera[20], Sz. Csizmadia[20], M. Deleuil[16], A. Erikson[20], S. Ferraz-Mello[21], E. W. Guenther[22], T. Guillot[5], S. Grziwa[23], A. Hatzes[22], G. Hébrard[24], T. Mazeh[25], M. Ollivier[6,17], H. Parviainen[26], M. Pätzold[23], H. Rauer[20,27], D. Rouan[17], A. Santerne[16], and J. Schneider[28]

(Affiliations can be found after the references)

Received 1 December 2017 / Accepted 1 September 2019

ABSTRACT

Aims. We report the discovery as well as the orbital and physical characterizations of two new transiting giant exoplanets, CoRoT-30 b and CoRoT-31 b, with the CoRoT space telescope.
Methods. We analyzed two complementary data sets: photometric transit light curves measured by CoRoT, and radial velocity curves measured by the HARPS spectrometer. To derive the absolute masses and radii of the planets, we modeled the stars from available magnitudes and spectra.
Results. We find that CoRoT-30 b is a warm Jupiter on a close-to-circular 9.06-day orbit around a G3V star with a semi-major axis of about 0.08 AU. It has a radius of $1.01 \pm 0.08\ R_J$, a mass of $2.90 \pm 0.22\ M_J$, and therefore a mean density of 3.45 ± 0.65 g cm^{-3}. The hot Jupiter CoRoT-31 b is on a close-to-circular 4.63-day orbit around a G2 IV star with a semi-major axis of about 0.05 AU. It has a radius of $1.46 \pm 0.30\ R_J$, a mass of 0.84 ± 0.34 M$_J$, and therefore a mean density of 0.33 ± 0.18 g cm^{-3}.
Conclusions. Neither system seems to support the claim that stars hosting planets are more depleted in lithium. The radii of both planets are close to that of Jupiter, but they differ in mass; CoRoT-30 b is ten times denser than CoRoT-31 b. The core of CoRoT-30 b would weigh between 15 and 75 Earth masses, whereas relatively weak constraints favor no core for CoRoT-31 b. In terms of evolution, the characteristics of CoRoT-31 b appear to be compatible with the high-eccentricity migration scenario, which is not the case for CoRoT-30 b. The angular momentum of CoRoT-31 b is currently too low for the planet to evolve toward synchronization of its orbital revolution with stellar rotation, and the planet will slowly spiral-in while its host star becomes a red giant. CoRoT-30 b is not synchronized either: it looses angular momentum owing to stellar winds and is expected reach steady state in about 2 Gyr. CoRoT-30 and 31, as a pair, are a truly remarkable example of diversity in systems with hot Jupiters.

Key words. planetary systems – stars: fundamental parameters – stars: individual: CoRoT-30 – stars: individual: CoRoT-31

1. Introduction

The Convection, Rotation and planetary Transits (CoRoT), a joint project of France, Austria, Belgium, Brazil, ESA, Germany, and Spain, was a low-Earth-orbit visible photometer designed to measure stellar light curves (LCs) for two main astrophysical programs: asteroseismology, and exoplanet detection (Baglin et al. 2006). Instrument characteristics and inflight performance can be found in Auvergne et al. (2009). CoRoT was launched on December 27, 2006, and was operated by the French Centre National d'Études Spatiales (CNES) until November 2, 2012, when an electrical failure stopped the observational program.

As for other transit surveys, the successful identification and characterization of planet candidates detected with CoRoT implies follow-up observations. Our ground-based photometric and velocimetric follow-up programs are described by Deeg et al. (2009) and Santerne et al. (2011), respectively.

According to prevailing theories of planet formation by core nucleated instability, close-in giant planets ($a \lesssim 0.1$ AU) cannot form in situ. This paradigm requires that gas giant planets migrate over one to two orders of magnitude in semi-major axis to produce the observed close-in giant planet population. Multiple scenarios for giant planet migration have been proposed, but they can be simplified into two broad categories: on one hand, migration may predominantly occur through interactions with the protoplanetary disk (Lin et al. 1996); on the other hand, the orbit of the proto-hot Jupiter could have been perturbed by another body onto a highly eccentric orbit, and subsequently shrank and was circularized by tidal dissipation (Rasio & Ford 1996). To date, there is no consensus on the dominant migration mechanism or whether there is migration at all. The number of super-Earth candidates detected at periods shorter than about 100 days by the *Kepler* telescope, and the abundance of tightly packed inner planets in the same data set, has recently led some authors to consider the possibility that hot and warm Jupiters, as well as close-in super-Earths, could indeed form in situ (Boley et al. 2016; Batygin et al. 2016). In particular, Batygin et al. (2016) have shown that the in situ formation scenario predicts that hot Jupiters have exterior

* Radial velocity measurements for CoRoT-30 and CoRoT-31 are also available at the CDS via anonymous ftp to cdsarc.u-strasbg.fr (130.79.128.5) or via http://cdsarc.u-strasbg.fr/viz-bin/cat/J/A+A/635/A122

super-Earth companions on either coplanar or highly inclined orbits. Alternatively, hot Jupiters without super-Earth companions are statistically expected to have higher core masses. It is therefore not enough to detect exoplanets, it is essential to precisely characterize their orbital and physical parameters to test formation and migration scenarios.

The known exoplanets with precisely measured masses and radii are still tainted by observational biases and statistically limited. Accurately measuring the masses and radii of close-in exoplanets and the properties of their host stars therefore remains very relevant today. The comparatively strong signals of close-in giant planets in radial velocity and photometry currently make them the planets with the highest relative accuracy on the planetary mass, radius, and density by far. This provides the most stringent physical constraints for all planets known outside the solar system, and combined with their good discovery statistics, offers the best perspectives for theoretical advances in the coming years.

In this article, we report the discovery of two transiting giant planets orbiting G stars, CoRoT-30 b and CoRoT-31 b, whose orbital and physical parameters we measured. We start by describing our photometric and spectrometric data sets for each planet (Sects. 2 and 3) and analyze the spectrum of the host star (Sect. 4), then we proceed to jointly model the light and radial velocity curves (Sect. 5), as well as the star (Sect. 6), in order to create to full models of the two planetary systems (Sect. 7). We conclude with a discussion (Sect. 8). A short appendix gives more details about the photometric contamination by neighboring stars.

2. Photometric observations

2.1. CoRoT-30

CoRoT-30 is one of the 5 722 target stars observed by CoRoT for 81 days during the seventh long run in constellation Aquila from 2011 April 5 to 2011 June 30 (LRc07 for short). This star belongs to the subset of 3401 MON stars for which a single LC is available (MON stands for monochromatic). Figure 1 (top) shows the photometric mask used by CoRoT to produce the LC superimposed on a Palomar Observatory Sky Survey (POSS) image of the sky. The stars were identified by query of Exodat, the CoRoT entry database (Deleuil et al. 2009). Because the fluxes of several neighboring stars leak into the photometric masks (Fig. A.1), their contributions were computed based on the procedure described by Bordé et al. (2010), but improved in the following way: the models for the stellar point spread functions (PSFs) were chosen according to the stellar colors. Moreover, an uncertainty on the sum of the contaminating fluxes was estimated through Monte Carlo simulations where the magnitudes, colors, and positions of the contaminants were randomly varied (10^4 draws). This procedure yielded a normally distributed contamination of $16.6 \pm 3.7\%$. The LC presented and analyzed here corresponds to version 3.0 of the data processed with version 2.0 of the CoRoT pipeline (Fig. 2, top). Out of 137 922 measurements, we chose to keep 121 736 measurements that were flagged as valid (total duration of 81.21 days) and are composed of a group of 3598 measurements with 512 s exposures (31.82 days), followed by a group of 118 138 measurements with 32 s exposures (49.38 days). Most invalid data are due to the South Atlantic Anomaly (see Chaintreuil et al. 2016, in the CoRoT Legacy Book, for all cases of invalid data). Running the algorithm described by Bordé et al. (2007) on this LC results in the detection of a train of 3.7 h transits with a period of 9.06 d,

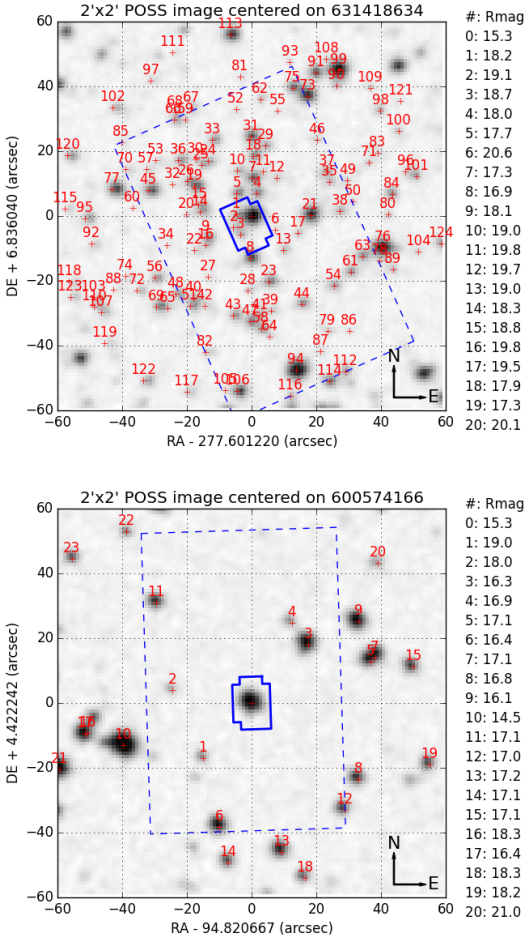

Fig. 1. POSS red image with neighboring stars numbered according to their distances to the target (number 0) for CoRoT-30 (*top*) and CoRoT-31 (*bottom*). The CoRoT mask is superimposed in blue, as well as the boundary of the CoRoT thumbnail image (blue dashed line).

that started 5.42 d after the beginning of LRc07 (Fig. 3). The signal-to-noise ratio (S/N) is 98.

Photometric follow-up observations of CoRoT-30 were performed in order to ascertain the absence of contaminating eclipsing binaries close to the target following the precepts of Deeg et al. (2009), and in order to improve the precision of the planetary ephemeris. A first follow-up in ON/OFF mode, acquiring short time-series during and outside of a predicted transit, was undertaken with the IAC 80 cm telescope of Teide Observatory, Tenerife, on 2011 September 5 (ON) and September 24 (OFF). These observations showed that the transit occurs on the target, and they excluded nearby faint stars that might be bright enough to also cause the signal found by CoRoT. CoRoT-30 was observed again on 2014 July 22 with the same telescope, and this time, a full transit was acquired. An estimate of the transit center time was obtained from determination of the midpoint between the steepest part of the ingress and egress slopes, at BJD 2456861.480 ± 0.005. This method was chosen over the more common fitting to transit models because it is more robust against errors arising from the asymmetric transit shape, most likely due to strongly varying seeing during observations. Based on the combination of CoRoT transits and this reobservation, a period of $9.060347 \pm 3.9 \times 10^{-5}$ days was derived.

The photometry was extracted with aperture photometry using vaphot/vanaliz (Deeg & Doyle 2013). This software performs differential photometry either within apertures whose

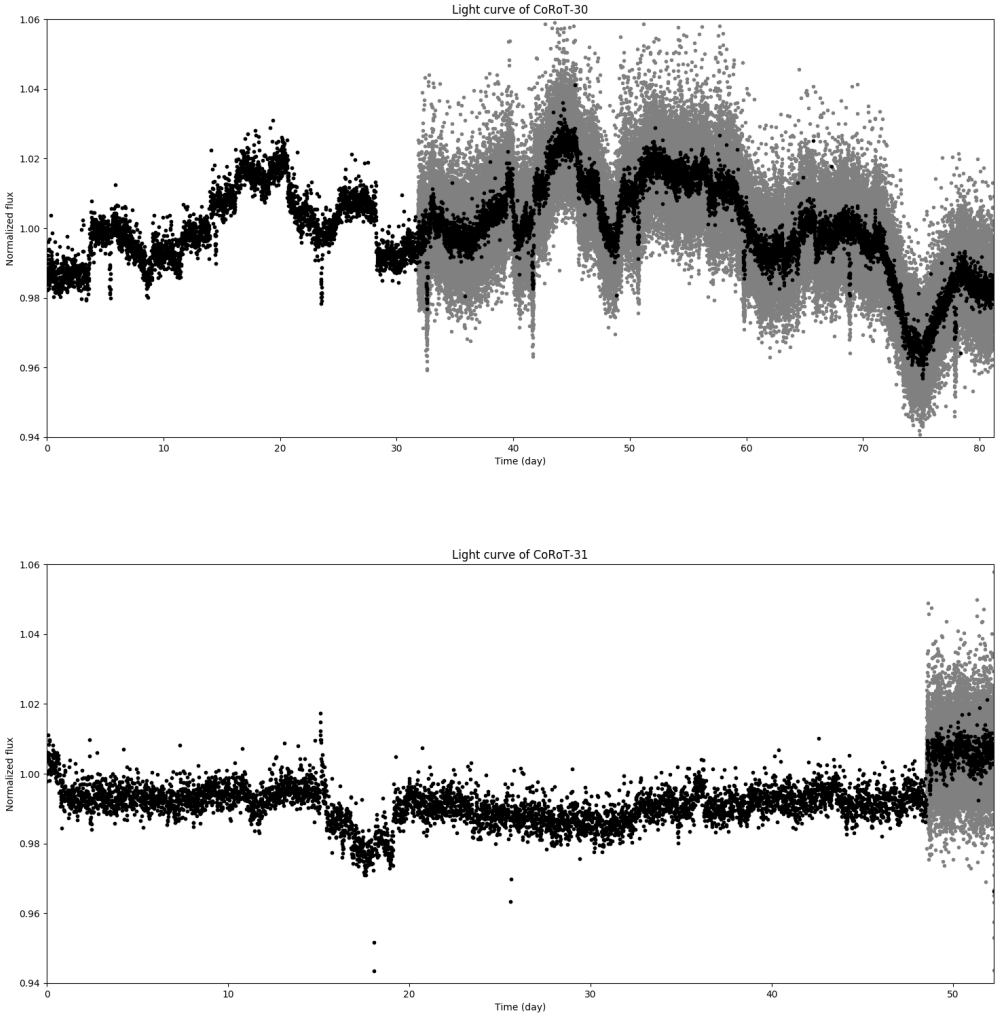

Fig. 2. Normalized light curves of CoRoT-30 (*top*) and CoRoT-31 (*bottom*) corrected for the contamination by the neighbors. The sampling period changes from 512 to 32 s after 31.8 days for CoRoT-30 and 48.5 days for CoRoT-31. An LC that is evenly rebinned at 512 s is overplotted in black.

sizes are scaled along the seeing variations during a time series, or uses fixed apertures throughout. Both methods were tried, and the better light curve, shown in Fig. 4, is based on fixed aperture sizes and was derived from a comparison with eight reference stars. This software has been used extensively during the photometric follow-up of the CoRoT mission and is considered as robust. Because of the poor weather conditions, the curve is relatively noisy, with an estimated point-to-point scatter of about 3 mmag, and a red component on a timescale of about 1 h and an amplitude of about 5 mmag.

2.2. CoRoT-31

CoRoT-31 is one of the 5588 target stars observed by CoRoT for 52 days during the seventh short run in constellation Monoceros (SRa04 for short) from 2011 October 7 to 2011 November 28. This star belongs to the subset of 4256 MON stars. As for CoRoT-30, Fig. 1 (bottom) shows the photometric mask used by CoRoT to produce the LC superimposed on a POSS image of the sky. In contrast to CoRoT-30, however, the flux leaks from neighboring stars into the mask of CoRoT-31 are negligible (Fig. A.2). The LC presented and analyzed here corresponds to version 3.0 of the data processed with version 2.3 of the CoRoT pipeline (Fig. 2, bottom). Out of 18 177 measurements, we chose to keep 14 569 measurements that were flagged as valid (total duration of 52.24 days) and are composed of a a group of 5650 measurements with 512 s exposures (48.52 days), followed by a group of 8919 measurements with 32 s exposures (3.71 days). Again, most invalid data are due to the South Atlantic Anomaly. Running the algorithm described by Bordé et al. (2007) on this LC resulted in the detection of a train of 3.3h transits with a period of $4.62941 \pm 7.5 \times 10^{-4}$ days that started 2.45 d after the beginning of SRa04 (Fig. 3). The S/N is 28.

3. Radial velocity observations

Radial velocity (RV) measurements of CoRoT-30 and CoRoT-31 were obtained with the HARPS spectrograph. HARPS is a cross-dispersed echelle spectrograph fiber-fed from the Cassegrain focus of the 3.6 m telescope at La Silla Observatory, Chile (Mayor et al. 2003). We obtained 18 and 17 spectra of CoRoT-30 and CoRoT-31, respectively, with exposure times ranging between 3300 and 3600 s. We used the high-accuracy mode (HAM), with spectral resolution $R \approx 115\,000$. For the observation of these faint targets, one of the two available fibers was set on the sky in order to monitor the moonlight and to obtain the best-fit sky background subtraction. The S/N per pixel at 550 nm ranges from 2.2 to 6.8 for CoRoT-30 and from 3.2 to 6.8 for CoRoT-31, which translates into photon noise uncertainties of about 30–40 m s^{-1} (Bouchy et al. 2001).

The spectra were reduced and extracted using the HARPS pipeline, and the RV was measured on each extracted spectrum by means of a weighted cross-correlation (Baranne et al. 1996; Pepe et al. 2002) with a numerical mask corresponding

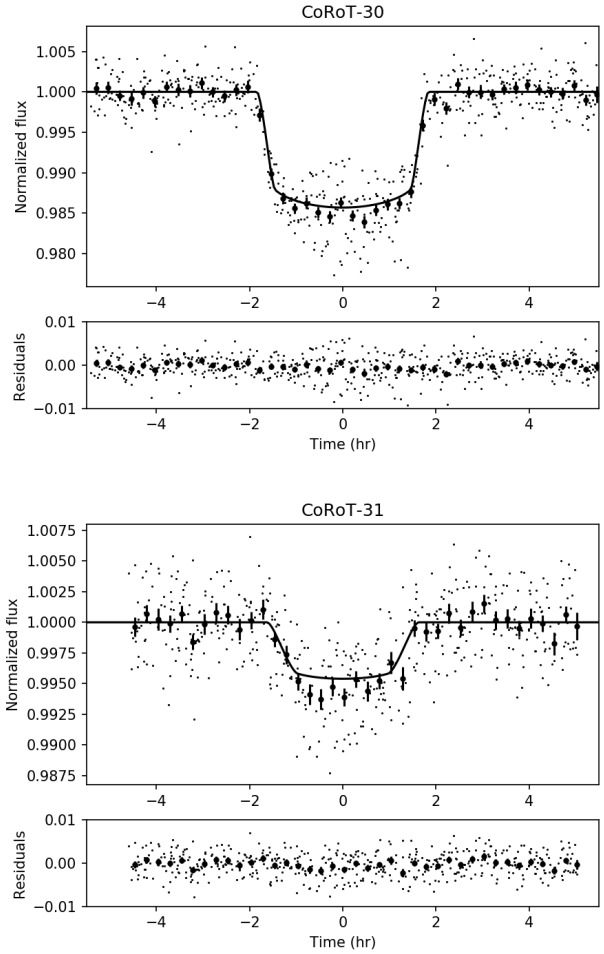

Fig. 3. Normalized transit light curve of CoRoT-30 (*top*) and CoRoT-31 (*bottom*). Large dots are 15 min averaged measurements. In both cases, the solid line shows the MAP model from Sect. 5.

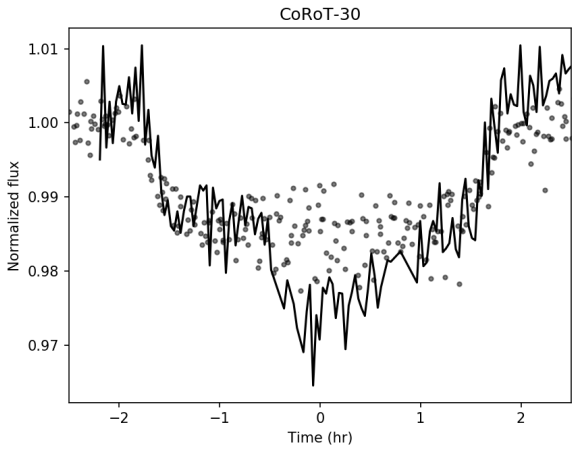

Fig. 4. Photometric follow-up observations of CoRoT-30 (solid line) on 2014 July 22 with the IAC 80 cm telescope of Teide Observatory, Tenerife. Observations with CoRoT (gray dots) from Fig. 3 are superimposed for comparison.

to a G2 star. The resulting cross-correlation functions (CCFs) were fit by Gaussians to obtain the RVs. The measured values are listed in Tables 1 and 2. Two spectra of CoRoT-31 were contaminated by moonlight (BJD − 2 450 000 = 5948.599 and BJD − 2 450 000 = 6238.824). In these spectra, we also measured the RVs after correction using the sky fiber, as described

Table 1. Radial velocity measurements on CoRoT-30 obtained by HARPS.

BJD −2 400 000	RV (km s^{-1})	1 σ error (km s^{-1})
56092.814780	−35.302	0.078
56097.815397	−34.660	0.072
56098.832797	−34.647	0.067
56099.745112	−34.842	0.110
56100.674800	−35.026	0.052
56101.632553	−35.212	0.048
56102.617123	−35.186	0.046
56116.623972	−34.641	0.045
56117.634238	−34.787	0.030
56121.641352	−35.155	0.048
56149.578742	−35.007	0.061
56150.679712	−34.899	0.071
56151.589788	−34.654	0.052
56158.544384	−35.091	0.055
56159.600057	−34.956	0.058
56477.696475	−34.629	0.057
56508.613572	−35.002	0.040
56518.630176	−35.159	0.040

Notes. BJD is the Barycentric Julian Date.

Table 2. Radial velocity measurements on CoRoT-31 obtained by HARPS.

BJD −2 400 000	RV (km s^{-1})	1σ error (km s^{-1})
55 925.704078	18.741	0.030
55 928.760898	18.547	0.048
55 942.729225	18.549	0.036
55 946.595486	18.512	0.041
55 948.599382	18.736	0.087 (†)
55 949.695427	18.732	0.039
55 950.706265	18.612	0.028
55 952.730171	18.633	0.043
55 953.723032	18.654	0.048
56 236.765837	18.818	0.031
56 237.772156	18.572	0.053
56 238.824323	18.551	0.093 (†)
56 243.809218	18.524	0.036
56 248.845617	18.570	0.030
56 250.716543	18.691	0.037
56 253.703517	18.534	0.031
56 255.685327	18.405	0.042

Notes. BJD is the Barycentric Julian Date. (†)Uncertainty increased due to contamination by moonlight (see text for details).

in Bonomo et al. (2010). Differences of 80 and 87 m s^{-1} were found between the two velocity measurements. These values were added quadratically to the uncertainty of each point. These observations are marked in Table 2.

Bisector analysis. The reflex motion produced by a planetary-mass companion induces a shift of the stellar spectral lines without changing their shapes. Variations in the bisector of the CCF can reveal a set of stellar lines that is blended with the lines from the main target star. Detection of such variations

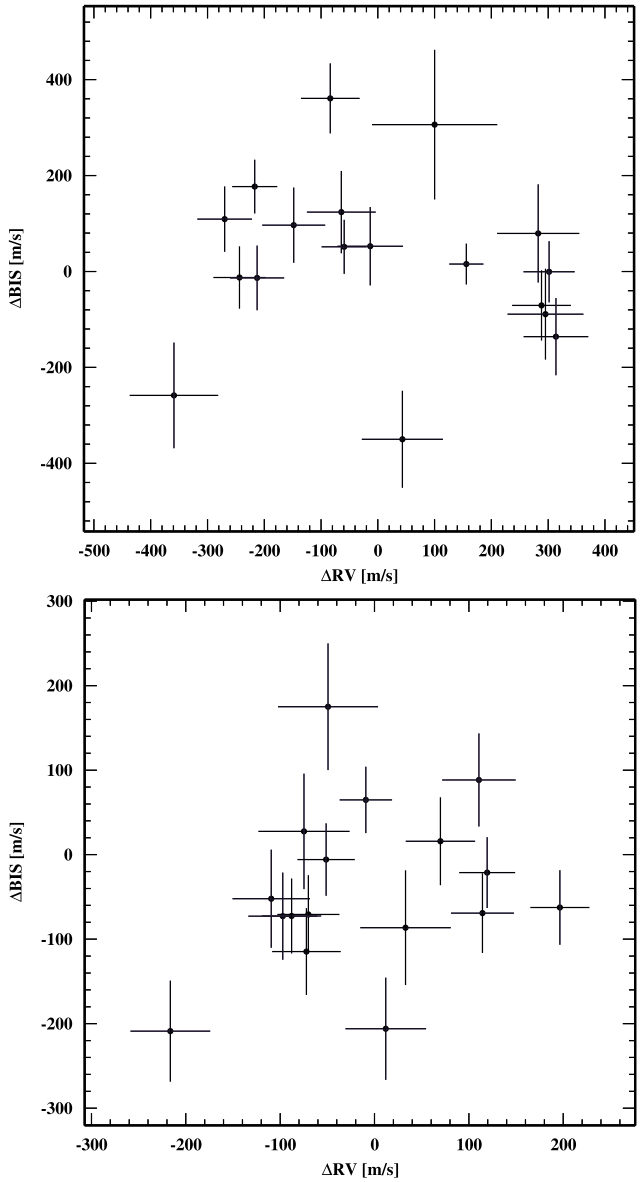

Fig. 5. Bisector velocity span measurements for CoRoT-30 (*top*) and CoRoT-31 (*bottom*).

in phase with the RV variations is usually seen as a strong sign that the transiting candidate is a false positive (e.g., Queloz et al. 2001). Stellar activity can also produce bisector velocity variations over the timescale of the rotational period of the star (e.g., Boisse et al. 2011).

The bisector velocity span measurements of CoRoT-30 and CoRoT-31 are presented in Fig. 5, where we assumed that the photon noise on the bisector is twice that of the RV measurement (Santerne et al. 2015). The bisector variations of CoRoT-30 may seem to correlate with respect to the RV variations. To test this, we performed the Bayesian comparison between the null hypothesis, that is, the bisector is constant with respect to the RV, to two competing explanations of the data: the bisector follows a linear or quadratic relationship with the RV measurements. In other words, the model is

$$\Delta\mathrm{BIS} = \alpha + \beta\,\Delta\mathrm{RV} + \gamma\,(\Delta\mathrm{RV})^2\,, \tag{1}$$

where $\beta = \gamma = 0$ under the null hypothesis, and $\gamma = 0$ under the linear model. To perform the comparison, we set priors not only on the model parameters but also on the different hypotheses. We assumed equal prior probabilities for the three competing hypotheses, and set uniform priors for all parameters, as listed in Table 3.

Table 3. Prior distributions on the model parameters for the relation between radial velocity and bisector span.

Parameter		Prior
α	[m s^{-1}]	$\mathcal{U}(-6, 6)$
β	[m^2 s^{-2}]	$\mathcal{U}(-3, 3)$
γ	[m^3 s^{-3}]	$\mathcal{U}(-0.05, 0.05)$

Notes. $\mathcal{U}(x_{\min}, x_{\max})$ is a uniform distribution between $x_{\min}$ and $x_{\max}$.

Because the prior volume is relatively small in the three models, we estimated the marginal likelihood using the mean estimator (see Kass & Raftery 1995), which approximates the marginal likelihood as the average likelihood function over a sample drawn from the prior distribution:

$$\widehat{\mathcal{Z}} = \frac{1}{N}\sum_{i=1}^{N} \mathcal{L}\left(\theta^{(i)}\right), \tag{2}$$

where $\{\theta^{(i)}\}$ is a sample drawn from the prior distribution. This estimator is usually very inefficient in high-dimensional spaces, where the (hyper-)volume containing significant likelihood mass is extremely small, but it is good enough in this case, and we found that the estimator converges correctly. The prior sample has 10 000 elements, and the computation was repeated 100 times to estimate the variance of the estimator. The uncertainties in the independent variable (RV) were accounted for when we constructed the likelihood function in Eq. (2) as described by Gregory (2005).

Under this prior choice, we found that for CoRoT-30, the null hypothesis is 4.63 ± 0.18 and 330 ± 115, which is more probable than the linear and quadratic hypotheses, respectively, where the reported values are the distribution mean and standard deviation. For CoRoT-31 we find posterior odds ratios of 6.59 ± 0.19 and 75 ± 11 between the constant model and the linear and quadratic ones, respectively. The null hypothesis is therefore the most probable model for both candidates.

On the other hand, the odds ratios are lower than the usually accepted limits defined by Kass & Raftery (1995) required to reject a hypothesis. However, we recall that first, this value depends strongly on the priors presented in Table 3. For example, doubling the prior width on the linear parameter approximately doubles the odds ratio in favor of the constant model, as expected: we derive 9.29 ± 0.54 and 13.22 ± 0.55 for CoRot-30 and CoRoT-31, respectively. Second, the limits presented by Kass & Raftery (1995) are commonly used when the possibility of rejecting a null hypothesis in favor of an alternative, more complex model is explored. In this case, the inverse happens. As the linear and quadratic models effectively contain the constant model, that is, they are nested, having posterior odds above unity is sufficient to claim that the null hypothesis cannot be rejected. In other words, including additional terms (β and γ different from zero) in Eq. (1) is not justified by the data.

We therefore conclude that no significant bisector variation is detected. Although variations of the bisector velocity span smaller than our uncertainties might still exist, this fact increases our confidence that the planetary hypothesis can explain the transits and the RV variations.

Table 4. Photospheric parameters of CoRoT-30 and CoRoT-31.

Photospheric parameters	CoRoT-30	CoRoT-31
Effective temperature $T_{\rm eff}$ (K)	5650 ± 100	5700 ± 120
Surface gravity $\log g$ ($\log_{10}$ cm s^{-2})	4.40 ± 0.10	3.85 ± 0.25
Iron abundance [Fe/H] (dex)	0.02 ± 0.10	0.00 ± 0.10
Microturbulent velocity [(a)] $v_{\rm micro}$ (km s^{-1})	1.0 ± 0.1	1.0 ± 0.1
Macroturbulent velocity [(a)] $v_{\rm macro}$ (km s^{-1})	2.1 ± 0.4	2.3 ± 0.4
Projected stellar rotational velocity $v \sin i$ (km s^{-1})	4.3 ± 0.4	2.8 ± 0.5
Spectral type [(b)]	G3 V	G2 IV
Photospheric lithium abundance [(c)] A(Li/H) (dex)	2.07 ± 0.14	2.26 ± 0.15

Notes. [(a)]Using the calibration equations of Bruntt et al. (2010). [(b)]With an accuracy of ± 1 subclass. [(c)]Defined as $A(\mathrm{Li/H}) = \log(n(\mathrm{Li})/n(\mathrm{H})) + 12$.

4. Spectral analysis

We derived the spectroscopic parameters of the host stars from the coadded HARPS spectra, which have an S/N per pixel at 550 nm of about 30 (CoRoT-30) and about 25 (CoRoT-31). The coadded spectra were obtained by shifting the HARPS spectra of CoRoT-30 and CoRoT-31 to the laboratory rest frame using the measured velocities and the known barycentric Earth RV at the time of the observation, and combining only those that were not contaminated by the scattered moonlight.

Following the procedures described in Fridlund et al. (2010) and Gandolfi et al. (2015), we carried out two independent analyses. The first analysis relies on the use of a customised IDL software suite, which fits the observed echelle data to a grid of theoretical model spectra calculated with the program SPECTRUM (Gray & Corbally 1994). We used ATLAS9 plane-parallel model atmospheres (Kurucz 1979), assuming local thermodynamic equilibrium (LTE) and solar atomic abundances as given in Grevesse & Sauval (1998). The second method relies on the use of the semi-automatic package spectroscopy made easy (SME, version 2.1; Valenti & Piskunov 1996; Valenti & Fischer 2005). SME is especially designed to determine photospheric stellar parameters from the match of the observed data to the synthetic spectra generated from the parameterized atmospheres. It uses a very large set of 1D LTE plane-parallel model atmosphere grids (Kurucz 1993, 2013; Hauschildt et al. 1999; Gustafsson et al. 2008).

We adopted the calibration equations from Bruntt et al. (2010) to estimate the microturbulent ($v_{\rm micro}$) and macroturbulent ($v_{\rm macro}$) velocities. We used the wings of the Balmer lines to estimate the effective temperature $T_{\rm eff}$, and the Mg I 516.7, 517.3, and 518.4 nm, the Ca I 616.2 and 643.9 nm, and the Na I D lines to determine the surface gravity $\log g$. The iron content [Fe/H] and the projected rotational velocity $v \sin i_\star$ were measured by fitting the profile of several clean and unblended iron lines.

The two spectral analyses provide consistent results well within the errors bars. The final adopted values are listed in Table 4. According to the calibration scale for dwarf and subgiant stars by Straizys & Kuriliene (1981), the effective temperatures of CoRoT-30 and CoRoT-31 translate into a G3 V and G2 IV spectral type, respectively.

The HARPS spectra of the two stars display moderately deep Li I 670.78 nm absorption doublets (Fig. 6). We estimated the photospheric lithium abundance by fitting the Li doublets using ATLAS9 LTE model atmospheres, while fixing the stellar parameters to the values listed in Table 4. Adopting the correction for non-LTE effects from Lind et al. (2009), we measured a lithium abundance of $A(\mathrm{Li/H}) = 2.07 \pm 0.14$ for CoRoT-30 and 2.26 ± 0.15 for CoRoT-31. The lithium abundance A(Li/H) is expressed with respect to hydrogen, on a scale in which the log of the abundance of hydrogen is set to 12.0, i.e., $A(\mathrm{Li/H}) = \log(n(\mathrm{Li})/n(\mathrm{H})) + 12$.

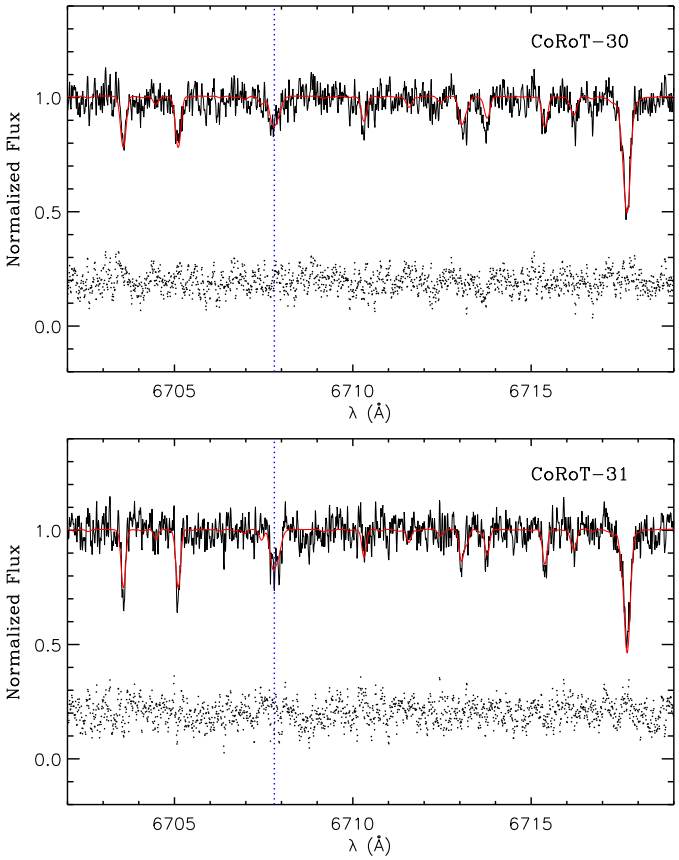

Fig. 6. HARPS coadded spectra of CoRoT-30 and CoRoT-31 (black lines), encompassing the Li I 670.78 nm absorption doublet. The best-fitting ATLAS9 spectra are overplotted with thick red lines. The vertical dashed lines mark the position of the Li doublet. The lowest part of the plots displays the residuals to the fit.

5. Data modeling

We used the PASTIS package (Díaz et al. 2014) to model the photometric and velocimetric data. In this package, the RV model assumes a standard Keplerian orbit and the LC model is computed with a modified version of the EBOP code

Table 5. Prior distributions for the model parameters.

Model parameters	Prior distribution	
	CoRoT-30	CoRoT-31
Planet period, P (days)	$\mathcal{N}(9.0601, 8\times10^{-4})$	$\mathcal{N}(4.6295, 0.0039)$
Transit epoch, T_0 (BJD-2 455 000)	$\mathcal{N}(665.515, 0.006)$	$\mathcal{N}(843.9442, 0.031)$
Radius ratio, R_p/R_*	$\mathcal{J}(0.01, 0.5)$	$\mathcal{J}(0.01, 0.5)$
Scaled semi-major axis a/R_*	$\mathcal{U}(2, 50)$	$\mathcal{U}(2, 20)$
Orbital inclination, i (deg)	$\mathcal{S}(70, 90)$	$\mathcal{S}(70, 90)$
RV semi-amplitude, K (km s^{-1})	$\mathcal{U}(0, 1)$	$\mathcal{U}(0, 1)$
Eccentricity, e	$\mathcal{U}(0, 1)$	$\mathcal{U}(0, 1)$
Argument of periastron, ω (deg)	$\mathcal{U}(0, 360)$	$\mathcal{U}(0, 360)$
Systemic velocity, γ (km s^{-1})	$\mathcal{U}(-35.1, -34.7)$	$U(18.45, 18.75)$
Linear limb-darkening coefficient, u	$\mathcal{U}(0, 1)$	$\mathcal{U}(0, 1)$
RV additional noise (m s^{-1})	$\mathcal{U}(0, 150)$	$\mathcal{U}(0, 150)$
LC additional noise (ppm)	$\mathcal{U}(0, 8000)$	$\mathcal{U}(0, 8000)$
LC out-of-transit relative flux	$\mathcal{U}(0.995, 1.005)$	$\mathcal{U}(0.995, 1.005)$
LC contamination	$\mathcal{N}(0.166, 0.037)$	–

Notes. $\mathcal{N}(\mu, \sigma)$: normal distribution with mean μ and standard deviation σ; $\mathcal{J}(x_{\min}, x_{\max})$: Jeffreys (log-flat) distribution between $x_{\min}$ and $x_{\max}$; $\mathcal{U}(x_{\min}, x_{\max})$: uniform distribution between $x_{\min}$ and $x_{\max}$; $\mathcal{S}(\theta_{\min}, \theta_{\max})$: sine distribution between $\theta_{\min}$ and $\theta_{\max}$.

(Nelson & Davis 1972; Etzel 1981; Popper & Etzel 1981) extracted from the JKTEBOP package (see Southworth 2011, and references therein). The stars were considered perfectly spherical with linear limb-darkening.

For both datasets, the log-likelihood function was constructed assuming uncorrelated normally distributed additive errors of two independent types: the first error, with known variance σ_i^2, describes the well-characterized instrumental noise for measurement i, and the second error, with unknown variance ϵ^2 identical for all measurements, describes all remaining unexplained effects of astrophysical (e.g., stellar variability) or instrumental origin:

$$\ln \mathcal{L} = -\frac{1}{2}\left(n_p + n_v\right)\ln(2\pi) - \frac{1}{2}\left(\sum_{i=1}^{n_p}\ln\left(\sigma_{p,i}^2 + \epsilon_p^2\right) + \sum_{j=1}^{n_v}\ln\left(\sigma_{v,j}^2 + \epsilon_v^2\right)\right) - \frac{1}{2}\left(\chi_p^2 + \chi_v^2\right),$$

where n is the number of measurements in each dataset, where p and v is the subscript for photometric and velocimetric data, and where

$$\chi^2 = \sum_{i=1}^{n}\frac{r_i^2}{\sigma_i^2 + \epsilon^2},$$

with r_i the residuals.

The prior distributions chosen for the model parameters are listed in Table 5. We chose wide uninformative priors with wide bounds, except for the ephemeris parameters. For CoRoT-30, the contaminating flux was considered as an additional model parameter with a prior distribution equal to the normal distribution obtained in Sect. 2.

The multidimensional joint posterior distribution of the model parameters was sampled using the Markov chain Monte Carlo (MCMC) algorithm described in Sect. 4 of Díaz et al. (2014). For every model parameter, we report in Table 6 the maximum a posteriori (MAP) and the standard deviation of the corresponding parameter marginal posterior sample. Additionally, we report the 95% highest density interval (HDI), defined as the interval containing 95% of the marginalized distribution mass such that no point outside the interval has a higher density than any point within it.

The MAP models for the transits and RVs are shown in Figs. 3 and 7, respectively. There is a clear outlier in the CoRoT-31 b data set. Removal of the outlier leads to a larger amplitude of 123 ± 20. This value is in agreement with our determination, constituting a difference of less than 1σ when normal distributions are assumed for both determinations. As expected, the precision on the semi-amplitude improves from about 40 to 16%. However, we did not find any reason to remove it from the analysis: its S/N, moonlight contamination level, and other proxies where all nominal, and we therefore decided to retain it.

6. Stellar models

We compared the photometric and spectroscopic data of CoRoT-30 and CoRoT-31 from Tables 4 and 7 to stellar evolution and atmospheric models to infer their masses $M_\star$, radii $R_\star$, and ages $\tau_\star$. These properties combined with those derived from RV and light curves allow us to infer the planetary properties.

The method that we employed to determine the stellar properties from the models involves two steps: (1) we used model stellar atmospheres to fit the photometric spectral energy distribution to derive the stellar angular diameter, θ, and (2) the observed spectroscopic properties and θ were compared with model properties from a grid of stellar evolution models to derive the mass, radius, age, and distance to the star. These two steps are described in detail as follows:

6.1. Fitting the spectral energy distribution of the host

We used the Levenberg–Marquardt minimization algorithm to fit theoretical photometric data calculated using the BASEL library of stellar atmospheres (Lejeune et al. 1997a,b) to the photometric magnitudes. The theoretical photometric data were calculated as follows. Filter transmission curves for the relevant filters were retrieved from the literature. We multiplied each of the filter transmission curves by the model spectrum that corresponded

Table 6. Star and planet characteristics of the CoRoT-30 and CoRoT-31 systems.

	CoRoT-30	CoRoT-31
Data from catalogs		
CoRoT-ID	631418634	600574166
CoRoT-WinID	LRc07-E2L-4905	SRa04-E2L-2567
PPMXL	5483892006672658120	2785130179564429581
USNO-B1	0968-0410581	0855-0078347
2MASS	18302427+0650094	06191697-0425201
Gaia DR2	4477300378701511296	3020494716521521152
Coordinates (J2000)	18:30:24.264 +06:50:09.424	06:19:16.975 -04:25:20.194
Magnitudes B, V, *Gaia*, R, I	16.55, 15.65, 15.41, 15.27, 14.75	17.03, ... , 15.47, 15.06, 14.59
Gaia parallax (mas)	0.942 ± 0.043	0.470 ± 0.038
Results from stellar modeling		
Star radius, $R_\star$ ($R_\odot$)	$0.91^{+0.09}_{-0.03}$	$2.15^{+0.56}_{-0.66}$
Star mass, $M_\star$ ($M_\odot$)	$0.98^{+0.03}_{-0.05}$	$1.25^{+0.22}_{-0.21}$
Star age (Gyr)	$3.0^{+3.7}_{-2.4}$	$4.7^{+4.7}_{-2.2}$
Star distance (pc)	960^{+68}_{-40}	2190 ± 710
Results from light curve and radial velocity combined analysis		
Planet period, P (day)	9.06005 ± 0.00024	4.62941 ± 0.00075
	[9.05955, 9.06051]	[4.62824, 4.63117]
Transit epoch, T_0 (BJD − 2 455 000)	665.5146 ± 0.0012	843.9445 ± 0.0044
	[665.5122, 665.5171]	[843.9346, 843.9523]
Radius ratio, $R_\mathrm{p}/R_\star$	0.1140 ± 0.0032	0.0699 ± 0.0076
	[0.1092, 0.1221]	[0.0561, 0.0787]
Scaled semi-major axis $a/R_\star$	21.0 ± 1.4	7.2 ± 2.9
	[16.5, 22.1]	[5.3, 16.5]
Impact parameter, b	0.00 ± 0.16	0.87 ± 0.27
	[0.00, 0.56]	[0.00, 0.90]
Orbital inclination, i (deg)	90.00 ± 0.56	83.2 ± 2.3
	[88.09, 90.00]	[82.5, 90.0]
Linear limb-darkening coefficient, u	0.28 ± 0.10	0.40 ± 0.26
	[0.08, 0.49]	[0.02, 1.00]
Systemic velocity, γ (km s^{-1})	-34.931 ± 0.014	18.604 ± 0.024
	[−34.962, −34.905]	[18.563, 18.657]
RV semi-amplitude, K (m s^{-1})	283 ± 20	88 ± 35
	[255, 335]	[22, 169]
Orbital eccentricity, e	0.007 ± 0.031	0.02 ± 0.16
	[0.000, 0.100]	[0.00, 0.48]
Argument of periastron, ω (deg)	178.1 ± 100.2	303.6 ± 107.9
	[0.0, 360.0]	[0.1, 359.8]
RV additional noise (m s^{-1})	7 ± 16	66 ± 21
	[0, 52]	[46, 132]
LC additional noise (ppm)	992 ± 157	291 ± 274
	[645, 1285]	[0, 968]
LC fractional contamination	0.160 ± 0.037	–
	[0.088, 0.239]	–
LC out-of-transit flux level (ppm)	60 ± 110	-40 ± 170
	[−53, 393]	[−323, 351]
Derived absolute physical parameters		
Planet mass, M_p (M_J)	2.90 ± 0.22	0.84 ± 0.34
	[2.49, 3.36]	[0.17, 1.52]
Planet radius, R_p (R_J)	1.009 ± 0.076	1.46 ± 0.30
	[0.930, 1.225]	[1.16, 2.21]
Planet density, ρ_p (g cm^{-3})	3.45 ± 0.65	0.33 ± 0.18
	[1.77, 4.33]	[0.00, 0.66]
Planet semi-major axis, a (AU)	0.0844 ± 0.0012	0.0586 ± 0.0034
	[0.0815, 0.0863]	[0.050, 0.065]

Notes. For the LC and RV combined analysis, the given values are the MAP and the standard deviation of the marginal posterior distribution of the parameters. In brackets we list the 95% highest density intervals (HDI) for the same distributions. HDI is defined as the interval containing 95% of the distribution mass, such that no point outside the interval has a higher density than any point within it.

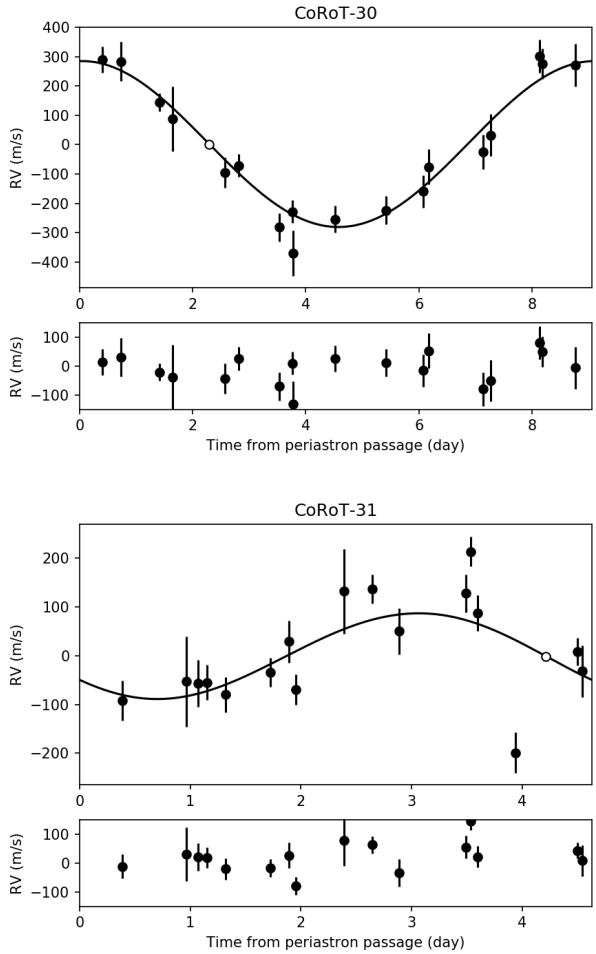

Fig. 7. Radial velocity curves for CoRoT-30 (*top*) and CoRoT-31 (*bottom*). White circles indicate transit times.

to the solar spectrum, scaled by $\frac{4}{3}\pi R_{\odot}^2$, to obtain the total flux f_λ, where λ refers to the filter band. Then its uncalibrated absolute magnitude in each band was calculated using the standard formula $-2.5 \log f_\lambda$. The true absolute V-band magnitude of the Sun is $M_V = 4.83$, and we adopted the colors of the Sun as given by Casagrande et al. (2012), Meléndez et al. (2010), and Ramírez et al. (2012b) in order to calculate the magnitudes in the other bands, given in Table 8. The solar absolute magnitudes were then subtracted from the uncalibrated magnitudes in order to obtain the zero-points. These zero-points were then used as the reference magnitudes in order to determine the absolute magnitudes of any star. The apparent magnitudes were then calculated using $m = M - \log d + 5$, where d is the distance to the star.

The apparent magnitudes (or fluxes) depend on knowing the stellar properties $T_{\rm eff}$, $\log g$, and [Fe/H], as well as $R_\star$ and d (and interstellar reddening). Because $R_\star$ and d have the inverse effect on the apparent magnitudes, we fit their ratio $R_\star/d = \theta$, the angular diameter of the star. Using an implementation of the Levenberg–Marquardt minimization algorithm, we can fit the four stellar properties, $T_{\rm eff}$, $\log g$, [Fe/H], and θ using the available multicolor photometry. In practice, we fixed $\log g$ and [Fe/H] at their observed spectroscopic values, and only fit $T_{\rm eff}$ and θ. Changing $\log g$ or [Fe/H] by a few σ has little effect on the final θ, but this is taken into account for the uncertainty in θ, see Creevey et al. (2015) for more detail.

The stars are faint. This implies that they are most likely quite distant, and certainly distant enough so that interstellar extinction is not negligible. Before we fit the photometric magnitudes to the model spectra, the spectra were reddened according to the coefficients of Cardelli et al. (1989), as given by the IDL routine `ccd_umred`. In general, we adopted the standard extinction law of $R_V = 3.1$, and we used as a fixed input the measured excess $E(B-V)$. After the model spectra were reddened, they were compared to the observed apparent magnitudes in the fitting process. The fitted θ are given in Table 9. These values are used as constraints in the second part of the analysis.

Table 7. Photometric data.

Filter	CoRoT-30	CoRoT-31
B	16.55 ± 0.1	17.03
V	15.65 ± 0.04	...
R	15.27 ± 0.03	15.06
I	14.75 ± 0.05	14.59
J	14.019 ± 0.029	13.908 ± 0.026
H	13.551 ± 0.037	13.469 ± 0.024
K_s	13.562 ± 0.045	13.426 ± 0.038
$E(B-V)$	0.15	0.4

Notes. Magnitudes and $E(B-V)$ derived from ExoDAT. When no error estimate existed, we adopted 0.5 magnitudes in the fitting method.

Table 8. Absolute photometric magnitudes of the Sun.

M_U	5.64
M_B	5.48
M_V	4.83
M_R	4.47
M_I	4.13
M_J	3.270
M_H	3.346
M_{K_s}	3.632
$M_{V,\rm Harris}$	4.854

Table 9. Derived angular diameters of the host stars given in milliarcseconds (mas).

	CoRoT-30	CoRoT-31
θ (mas)	0.00887 ± 0.00018	0.00954 ± 0.00024

Notes. The uncertainty also takes into account the variations in the results as we vary $E(B-V)$, $\log g$, and [Fe/H] by a few σ.

6.2. Stellar properties from a grid of models

We compared the observed properties $T_{\rm eff}$, $\log(g)$, $[M/H]$, θ, and (for CoRoT-30 alone) the observed mean stellar density $\rho_\star = 1.25^{+0.23}_{-0.28}\,\rho_\odot$ to grids of stellar models. For CoRoT-31, the density $\rho_\star = 0.87^{+0.80}_{-0.54}\,\rho_\odot$ does not provide a constraint. We used two sets of models: the first set, which we adopted as the reference, contained the BASTI stellar evolution models[1] (Pietrinferni et al. 2004). The second, which was used to test for systematic effects, is our own set that we constructed using the ASTEC stellar evolution code (Christensen-Dalsgaard 2008). ASTEC is used in the following configuration: the EFF equation of state (Eggleton et al. 1973) without Coulomb corrections, the OPAL opacities (Iglesias & Rogers 1996) supplemented by Kurucz

[1] http://basti.oa-teramo.inaf.it/index.html

Table 10. Stellar parameters of CoRoT-30 and CoRoT-31 from evolution models.

Star	$R_\star$ ($R_\odot$)	$M_\star$ ($M_\odot$)	$\tau_\star$ (Gyr)	$L_\star$ ($L_\odot$)	$T_{\rm eff}$ (K)	$\log g$	$\rho_\star$ ($\rho_\odot$)	d (pc)
CoRoT-30	$0.91^{+0.09}_{-0.03}$	$0.98^{+0.03}_{-0.05}$	$3.0^{-2.4}_{+3.7}$	$0.77^{+0.22}_{-0.09}$	5660^{+107}_{-90}	$4.51^{-0.06}_{+0.03}$	$1.07^{-0.12}_{+0.06}$	960^{+68}_{-40}
CoRoT-31	$2.15^{+0.56}_{-0.66}$	$1.25^{+0.22}_{-0.21}$	$4.7^{-2.2}_{+4.7}$	$4.5^{+2.2}_{-2.3}$	5730^{+99}_{-126}	$3.87^{-0.13}_{+0.24}$	$0.63^{-0.16}_{+0.30}$	2190^{+710}_{-710}

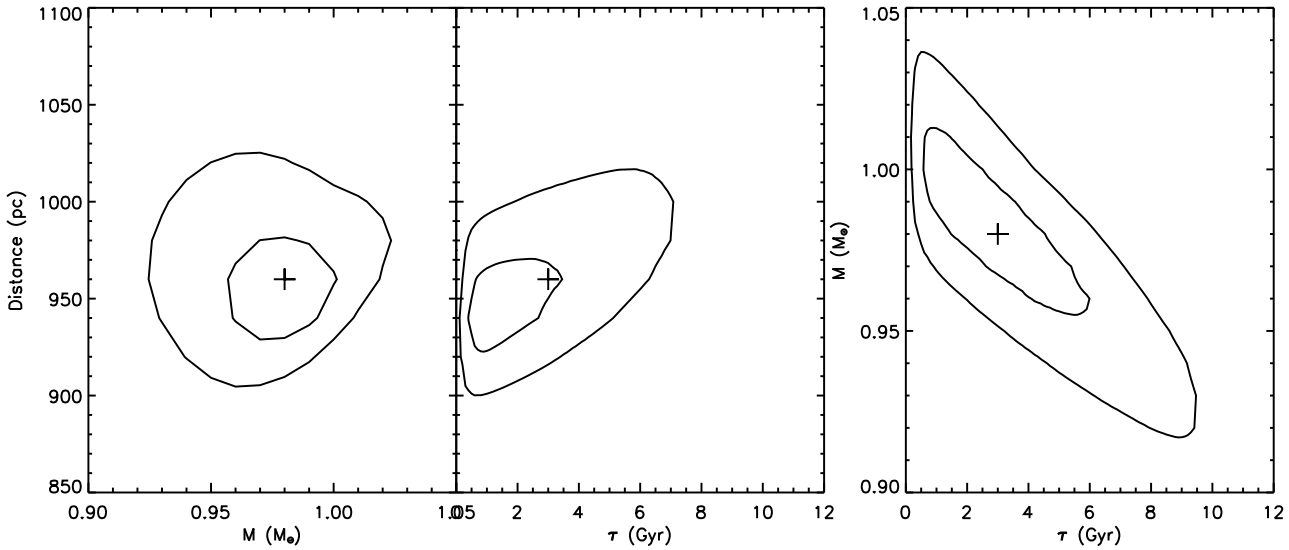

Fig. 8. Contour plots for CoRoT-30 showing the correlations between mass, age, and distance at a fixed metallicity. The most likely value is indicated by the cross. The contours are only indicative of the correlations and are shown for 50 and 85% of the maximum height.

opacities at low temperatures, solar mixture from Grevesse & Noels (1993), and nuclear reaction rates from Bahcall & Pinsonneault (1992). Convection in the outer convective envelope is described by the mixing-length theory of Böhm-Vitense (1958), and this is characterized by a variable parameter $\alpha_{\rm MLT}$ (where $l = \alpha_{\rm MLT} H_{\rm p}$, l is the mixing length and $H_{\rm p}$ is the pressure scale height). When a convective core exists, there is an overshoot layer that is also characterized by a convective core overshoot parameter $\alpha_{\rm ov}$, and this is set to 0.25. Diffusion of helium is treated using the description by Michaud & Proffitt (1993).

We followed a Bayesian approach to estimate the stellar model parameters age, mass, and distance, using a fixed metallicity. Interpolation in metallicity is delicate, and for the BASTI models [Fe/H] around the solar metallicity (+0.06 dex), this is −0.25 and +0.26 dex. We computed their posterior probability densities (up to a normalization constant) with the likelihood

$$\mathcal{L}(\boldsymbol{x}_\star) = \frac{1}{(2\pi)^{N/2}\,\sigma_{1\ldots\sigma_N}} \exp\left[-\frac{1}{2}\sum_{i=1}^{N}\frac{(f(\boldsymbol{x}_\star, i) - f_i)^2}{\sigma_i^2}\right], \quad (3)$$

where $\boldsymbol{x}_\star$ is the vector of model parameters, $f(\boldsymbol{x}_\star, i)$ are the N model observables, and f_i and σ_i are the observations and their uncertainties.

For CoRoT-30, we imposed a prior from the Galactic disk age as follows:

$$P(\tau_\star) = \begin{cases} 1.0 & \text{if } \tau_\star < 8.8 \text{ Gyr}, \\ \exp\left(\frac{(\tau_\star - 8.8)^2}{2(1.7)^2}\right) & \text{if } \tau_\star \geq 8.8 \text{ Gyr}. \end{cases} \quad (4)$$

Additionally, to compensate for the unequal evolution timescales of stars of different masses (important for main-sequence stars), we imposed a prior that corrects for these effects based on the evolution speed $\left(\frac{\partial R}{\partial \tau}\right)^{-1}$. For the mass, we experimented with a prior based on Salpeter's initial mass function, but as it made no significant difference, we reverted to a uniform prior. For CoRoT-31, all priors were chosen uniform, that is, the posterior probabilities are proportional to the likelihood.

For CoRoT-30 (CoRoT-31), the posterior probability densities were calculated from a grid of models that spanned an age of 0.0–16.0 Gyr in intervals of 0.1 Gyr, a mass of 0.85–1.15 $M_\odot$ (0.85–1.60 $M_\odot$), in intervals of 0.01 $M_\odot$, and a distance of 700–1300 pc (400–3500 pc), in intervals of 10 pc.

After marginalizing over the other parameters, we defined the best estimate for a given parameter as the value corresponding to the maximum of the distribution. We calculated the 68% non-symmetric confidence interval and adopted this as our uncertainty. As a sanity check, we applied this approach to the solar observed properties $\{T_{\rm eff}, \log g, [M/H], \rho_\star\} = \{5800, 4.43, 0.0, 1.0\}$ (ignoring the angular diameter), using the BASTI grid. We obtained a mass of $1.00^{+0.03}_{-0.02}$ $M_\odot$, a radius of $1.01^{+0.03}_{-0.03}$ $R_\odot$, and an age of $4.80^{+1.6}_{-1.6}$ Gyr.

The results for CoRoT-30 and CoRoT-31 are summarized in Table 10. We derived a young age for CoRoT-30, that is, between 1.0 and 4.0 Gyr for a 1.00 to 0.96 $M_\odot$ star, consistent with its higher observed Li abundances and rotation period, while for CoRoT-31, we obtained an evolved star of about 5 Gyr and 1.25 $M_\odot$. Age, mass, and distance are correlated, as we show in Fig. 8 for CoRoT-30.

This work was originally conducted without knowing the *Gaia* parallax. However, it is worth noting that the derived radii, which depend on the inferred distances using our method, agree to within 1σ with the distances inferred using the *Gaia* parallax. For CoRoT-30, a parallax of 0.942 ± 0.043 mas yields

Table 11. Effect of different models and metallicity on the stellar radius and mass.

	$[M/H]$ (dex)	$R_\star$ ($R_\odot$)	$M_\star$ ($M_\odot$)
BASTI	+0.00	$0.93^{+0.07}_{-0.04}$	$0.97^{+0.04}_{-0.03}$
ASTEC	+0.00	$0.94^{+0.07}_{-0.05}$	$0.97^{+0.04}_{-0.03}$
ASTEC	+0.02	$0.94^{+0.08}_{-0.04}$	$0.98^{+0.04}_{-0.03}$
ASTEC	−0.08	$0.90^{+0.08}_{-0.04}$	$0.94^{+0.03}_{-0.03}$
ASTEC_{+Z}		$0.94^{+0.08}_{-0.06}$	$0.98^{+0.05}_{-0.04}$

Notes. The final row adds metallicity as a fourth dimension.

a distance of 1062^{+51}_{-46} pc, while for CoRoT-31, a parallax of 0.470 ± 0.038 mas yields a distance of 2128^{+187}_{-160} pc. For CoRoT-30 a slightly greater distance (e.g., $+1\sigma$) would imply a slightly larger radius, but it would still be well within the uncertainties we derive. For CoRoT-31, we agree.

For CoRoT-30 we explored the effects of metallicity on the parameters and the uncertainties using the ASTEC models, and the results for mass and radius are summarized in Table 11. Because the BASTI models do not have the exact same metallicity as CoRoT-30, we determined the mass and radius using the ASTEC models with solar metallicity to compare directly with the BASTI results, and with the observed [Fe/H] = +0.02 dex. The differences in the parameters are insignificant. However, when we assume a metallicity of −0.08 dex (-1σ), we bias the result toward a slightly lower mass and radius. We then extended the ASTEC grid to a fourth dimension to probe the effect of metallicity on the overall solution, and our parameter values did not change from the original values, but the uncertainties were higher by about 12%.

7. Models of CoRoT-30 and CoRoT-31 systems

With the completed data modeling in Sect. 5 and the stellar modeling in Sect. 6, we can convert relative quantities into absolute ones for the planets. For convenience, Table 6 summarizes all the quantities we measured or computed for the CoRoT-30 and CoRoT-31 systems.

We compared the density of CoRoT-30 b and CoRoT-31 b to the ensemble of synthetic planets produced by the CoRoT-Mark1 model (Broeg 2006, 2009). Mark1 planet models are evolved assuming hydrostatic equilibrium and constant mass with the equations and methods of Broeg & Benz (2012) and Broeg et al. (2010) and a 1 Myr exponential decay of nebula pressures and planetesimal accretion rate. The resulting Mark1R ensemble consists of time-dependent, quasi-static planet models with R(t) etc. for all Mark1 synthetic planets. The density evolution of all Mark1R models corresponding to the host type and planetary orbital period and that fit our planet-mass constraints are shown in Fig. 9, together with the age constraint and 1, 3, and 5σ density constraints.

A bundle of Mark1R models ($1\,M_\odot$, eight days) hits the CoRoT-30 b constraints within the 1σ error ellipse (red) and all models fitting the mass constraint are within about 2σ, although there is a trend towards the higher measured values. Models that fit all constraints contain cores from 15 to 75 $M_{\rm Earth}$.

Given the nature of the weaker mass constraint for the relatively heavy and inflated CoRoT-31 b, a wide and qualitatively different set of Mark1R-evolutions ($1\,M_\odot$, four days)

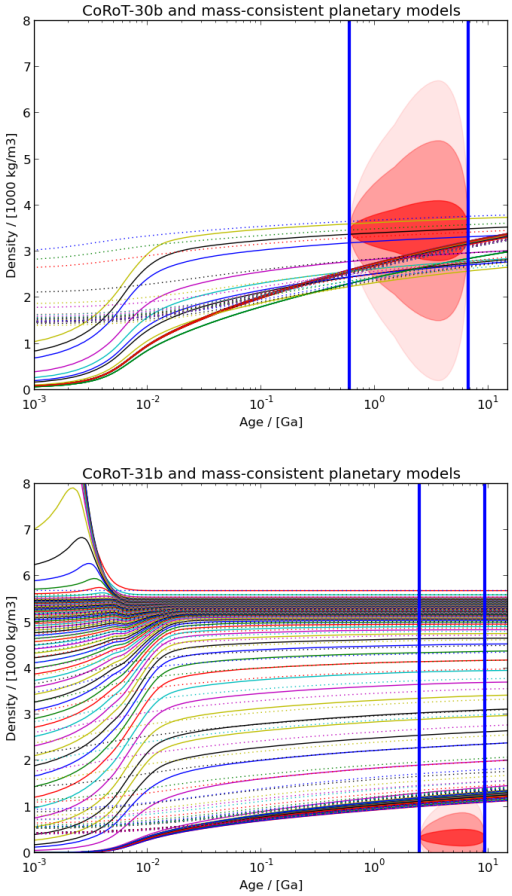

Fig. 9. Density evolution of quasi-hydrostatic Mark1R planetary models that fit the observational mass constraints for CoRoT-30 b (*top*) and CoRoT-31 b (*bottom*). Blue vertical lines mark the youngest and oldest inferred stellar ages. Red shaded ellipses fit the 1, 3, and 5σ limits for the planetary density at the inferred stellar ages. Full, dashed, and dotted lines mark planet models for high, medium, and low assumptions about the planetesimal accretion rate in the Mark1 ensemble.

were found. We highlight the contracting-expanding family at young ages in Fig. 9 below 10 Myr. The age and density constraints (red ellipses between the age limits) favor a bundle of low-density protoplanets that monotonically contract to the epoch of observation. The densest part of the bundle (highest track-density of Mark1R-models) somewhat favors the higher planetary densities near the 1σ limit of the observed values.

Both planets are consistent with a large number of these simple core-envelope planet formation-evolution models at the observed ages. This indicates that the core of CoRoT-30 b would weigh between 15 and 75 Earth masses, whereas relatively weak constraints favor no core for CoRoT-31 b. With their similar hosts and orbits, their radius difference of about 50%, their factor-of-three difference in mass and a density variation of about a factor of 10, CoRoT-30 b and -31 b are a remarkable example of planetary diversity (cf. Figs. 9 and 10). We have here a challenging diversity constraint that any theory of planet formation will have to include in the future.

8. Discussion

8.1. Formation and migration of giant planets

With an orbital period of 4.63 days, a mass of $0.84 \pm 0.34\,M_{\rm J}$, and a radius of $1.46 \pm 0.30\,R_{\rm J}$, CoRoT-31 b is a typical hot Jupiter

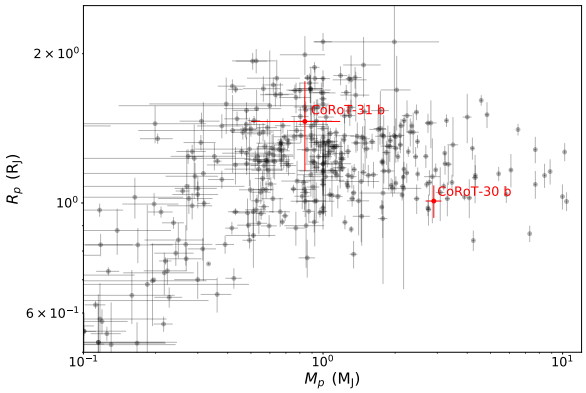

Fig. 10. Radius as a function of mass of characterized transiting giant exoplanets as of August 2019 (Han et al. 2014, see http://exoplanets.org/). The two planets presented in this paper are highlighted in red and labeled.

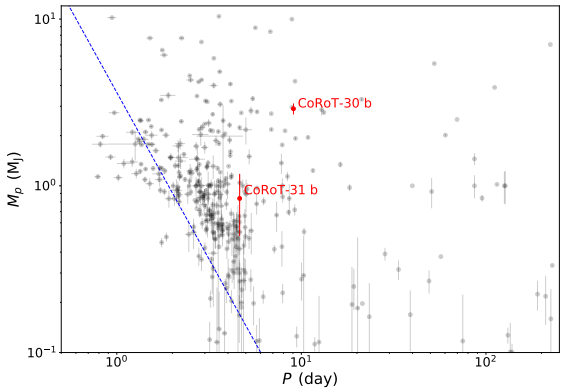

Fig. 11. Mass as a function of orbital period of characterized transiting giant exoplanets as of August 2019 (see http://exoplanets.org/). The two planets presented in this paper are highlighted in red and labeled. The dashed line represent the orbital period at twice the value of the Roche limit (for a host with one solar mass). This would be the final orbital period of an initially eccentric distant planet as a result of the high-eccentricity migration mechanism.

orbiting a slightly evolved solar-like star. The mass and radius of CoRoT-30 b, $M_p = 2.90 \pm 0.22\ M_J$ and $R_p = 1.01 \pm 0.08\ R_J$, are also typical of the population of well-characterized transiting planetary companions (Fig. 10).

This suggest that the formation of these two giant planets is similar to that of the other known close-in giant exoplanets. Using an albedo $A = 0$, the longer orbital period of CoRoT-30 b at 9 days yields an equilibrium temperature $T_{eq} = T_{eff}(1 - A)^{1/4}\sqrt{\frac{R_\star}{2a}} = 894 \pm 30$ K, however, so that CoRoT-30 b is at the transition between what is usually referred to as "hot" and "warm" Jupiters. Relatively few transiting giant planets are known in this range of orbital periods. Even when we extend the sample to include results of RV surveys, the number of detected giant planets at orbital periods greater than about 10 days decreases, followed by a sharp rise in their distribution outside of ~1 AU, the so-called period valley (Mayor et al. 2011; Santerne et al. 2016) that none of the proposed theories for planet formation and migration can fully explain. The careful measurements of orbital and physical parameters presented in this study enable us to place these two systems in the context of the known close-in planet population and discuss their implications for formation and migration theories.

Different migration scenarios predict different properties of the final orbit. The high-eccentricity migration mechanism (HEM) postulates that giant planets are formed at an orbital distance of several AU and are subsequently excited to a highly eccentric orbit through gravitational interactions with other bodies. Because of this high eccentricity, the distance between the planet and the star at periastron is a fraction of the semi-major axis. If this distance becomes smaller than the Roche limit, the planet is at risk of being torn apart by tidal forces. Thus it is reasonable to set the Roche limit as the lower bound for the initial periastron of the population of proto-hot Jupiters. There, the tides raised on the planet by the star are strong enough to quickly circularize the orbit. Assuming that circularization proceeds at constant orbital angular momentum, the relationship between the periastron distance of the initial eccentric orbit and the final circular orbit is simple. If circularization can take place without significant mass loss from the planet, it is straightforward to show that the final semi-major axis is expected to be twice the Roche limit (Ford & Rasio 2006).

Figure 11 shows the mass of characterized transiting giant exoplanets as of August 2019 as a function of orbital period. The orbital period corresponding to twice the Roche limit is indeed an approximate lower envelope for this population, advocating in favor of the HEM. CoRoT-31 b clusters with most known giant planets, but the long orbital period and high mass of CoRoT-30 b clearly set it apart. The circularization time t_{circ} can be approximated as in Ivanov & Papaloizou (2007) by

$$t_{circ} \sim 200 \left(\frac{M_p}{M_J}\right)^2 \left(\frac{M_\star}{M_\odot}\right)^{-2} \left(\frac{R_p}{R_J}\right)^{-8} \left(\frac{P}{3\ \text{days}}\right)^6 \sqrt{\frac{a_{init}}{10\text{AU}}}\ \text{Myr}, \quad (5)$$

where P is the current orbital period in days and a_{init} is the initial semi-major major of the proto-hot Jupiter. The initial semi-major axis here is the typical distance to the star where a giant planet can form by core-accretion in a disk, and could range between 1 and 100 AU. When this initial semi-major axis is taken to lie at 5 AU, CoRoT-31 b is compatible with the HEM with $t_{circ} \sim 50$ Myr, but CoRoT-30 b has $t_{circ} \sim 800$ Gyr, which strongly disfavors the high-eccentricity migration scenario in this case. Under the HEM hypothesis, all warm Jupiters are in the midst of tidal migration through tidal circularization. For CoRoT-30 b, as for many of the observed warm Jupiters, however, the eccentricities are too low to allow this process to take place on a reasonable timescale. Moreover, observations show that the expected population of super-eccentric migrating proto-hot Jupiters is missing (Dawson et al. 2015). Reconciling observations and the HEM scenario seems to demand that circularization should be both very fast and affect wider orbits, which would require a tidal dissipation mechanism in planets that is much more efficient than what is usually measured (in the solar system) or derived from theory. More observations of both hot and warm Jupiters, crucially with a better estimation of their age, would help place constraints on the HEM scenario.

8.2. Host star properties

The spectral analysis indicates that CoRoT-30 is a G3V star, with an effective temperature, surface gravity, and metallicity very similar to that of the Sun. Stellar models favor a solution slightly less massive than the Sun, but also slightly younger than the Sun. At $3.0^{3.7.8}_{-2.4}$ Gyr, the star is well within its main sequence and belongs to the parameter space where rotation rates can be used as an empirical age estimator (Jeffries 2014). Its high measured rotational velocity is not characteristic of solar-like stars of this

age ($v \sin i = 4.3 \pm 0.4$ km s^{-1}). Using this value and the radius determination from stellar models, we can obtain an upper limit on the rotation period of $10.7^{+1.5}_{-1.1}$ days. Using gyrochronology (Barnes 2007) and the magnitudes given in Table 7, this yields an age of about 535 ± 255 Myr, which is broadly in 1σ agreement within our inferred value. This would correspond to a solution at the higher end of our stellar mass estimation, however. To the accuracy of our measurements, two scenarios must be considered: either we have a star very similar to the Sun, but rotating faster than what is expected at its age, or our most likely value for the age of the star is overestimated, and we have a very young system that just begins on the main sequence. On the other hand, CoRoT-31 is also similar to the Sun in terms of effective temperature and metallicity, but its surface gravity makes it a subgiant star, which yields a spectral type of G2IV. Correspondingly, the stellar models return an age similar to the Sun's, but a higher mass. CoRoT-30 and CoRoT-31 are thus similar stars that differ in their evolutionary stage, one being on the main sequence, and possibly close to its beginning, while the other has already started to leave it.

The spectral analysis presented here provides us with another age estimator: the surface lithium abundance. Lithium is prone to destruction by proton capture at relatively low temperatures ($\sim 2.5 \times 10^6$ K) and the reaction is extremely temperature dependent ($\propto T^{20}$). Thus lithium depletion occurs mainly during the pre-main sequence, and for solar-like stars, surface lithium depletion should stop on the main sequence because by then the temperatures needed to burn it are just below the base of the convective zone. In the solar neighborhood, lithium abundances have been found to vary by two orders of magnitude, even for solar-like stars (Ramírez et al. 2012a), however. It seems that rotation-induced mixing and angular momentum loss are efficient mechanisms to destroy lithium in solar-type stars on the main sequence, but a fully consistent picture remains elusive (Amard et al. 2016). Notably, the presence of planets has been proposed as causing additional lithium depletion (Israelian et al. 2009; Chen & Zhao 2006). Two main mechanisms have been invoked, one related to planetary migration, the other to the velocity shear at the base of the convective zone caused by the locking of the disk to star. Because it is expected that planet formation requires a long-lived disk, stars hosting planets may have experienced longer disk-locking phase and increased rotational mixing, leading to enhanced lithium burning (Bouvier 2008). However, some authors deny any connection between low lithium abundance and planets, arguing that the sensitivity of the lithium abundance to other stellar parameters such as age and metallicity is responsible for the lithium abundance difference between stars with and without planets (Ramírez et al. 2012a).

Because they are very different in age and both host planets, it is interesting to discuss how CoRoT-30 and CoRoT-31 fit this picture. We took two catalogues of stars with measured lithium abundances that argue for a link between Li depletion and planets (Delgado Mena et al. 2014) and against it (Ramírez et al. 2012a) (Fig. 12). Both studies derived Li abundances by standard LTE spectral-line profile fitting of the region near the lithium resonance doublet at 6708 Å. The sample of Delgado Mena et al. (2014) has typical errors of about 53 K for $T_{\rm eff}$, 0.08 dex for $\log g$, and 0.05 dex for metallicity. The sample of Ramírez et al. (2012a) has typical errors of about 44 K for $T_{\rm eff}$, 0.11 dex for $\log g$, and 0.06 dex for metallicity. The former contains only solar-type stars in the main sequence, while the latter includes both younger and older stars. The lithium abundances derived by our analysis of CoRoT-30 and CoRoT-31 are corrected for non-LTE effects, but for this type of stars the non-LTE corrections are insignificant compared to the error bars (Lind et al. 2009).

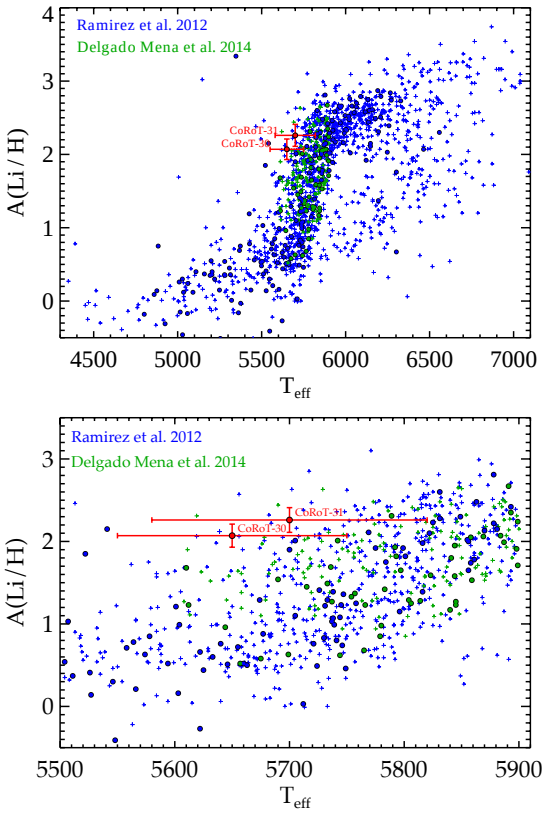

Fig. 12. Lithium abundance as a function of effective temperature. *Top*: catalogs provided by Ramírez et al. (2012a) (in blue) and Delgado Mena et al. (2014) in green, and we retain only the targets for which a definitive measure of A(Li/H) was possible (discarding targets with only upper limits, and stars in a binary system). The stars known to harbor a planet are shown by colored spots, and those without any detected companion are represented by crosses. The two systems presented in this paper are highlighted in red and labeled. *Bottom*: same data sets, but showing only stars with $5500 \leq T_{\rm eff} \leq 5900$.

CoRoT-30 and CoRoT-31 have higher lithium abundances than the other stars, both with and without planets. Unfortunately, the uncertainty we found in estimating the effective temperature limits the significance of the result. It is indeed enough to place the temperature of both stars at 1σ of their nominal values to reconcile them with lithium abundances of the corresponding stellar population. Moreover, CoRoT-31 is slightly evolved, so there are no equivalent stars in the sample of Delgado Mena et al. (2014), as we show in Fig. 13. Although the number of stars in this range of $\log(g)$ is quite small in the sample of Ramírez et al. (2012a), CoRoT-31 does not appear remarkably depleted compared to similar stars without detected planets. Similarly, CoRoT-30 has the high lithium abundance of stars younger than ~8 Gyr. Both systems do not seem to support the claim that stars hosting planets are more depleted in lithium. The number of stars in the sample is quite small, however, and more measurements of lithium abundances for stars with and without planet are required to reach definite conclusions.

8.3. Tidal evolution

We can investigate the tidal stability of the systems with the complete orbital and physical characterization presented here. The

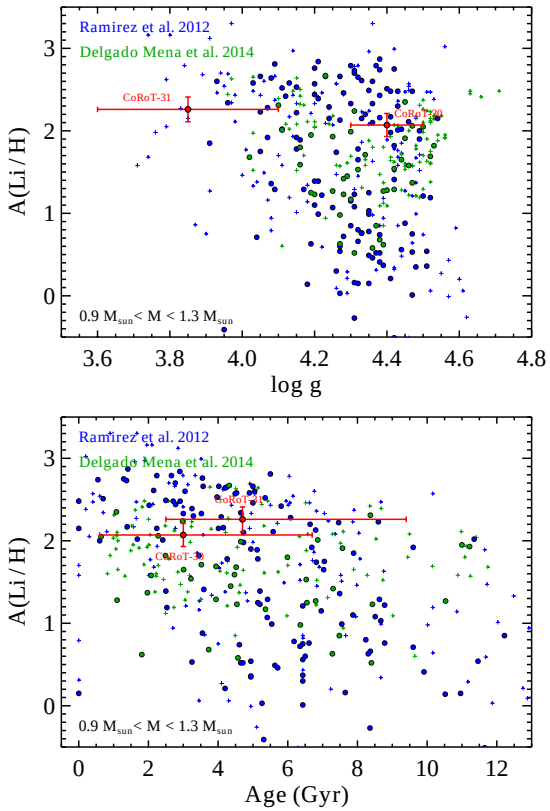

Fig. 13. Lithium abundance as a function of $\log(g)$ (*top*) and age (*bottom*). The sample shown in Fig. 12 is now limited to stars with $0.9 \leq M \leq 1.1\ M_{\odot}$. The two systems presented in this paper are highlighted in red and labeled.

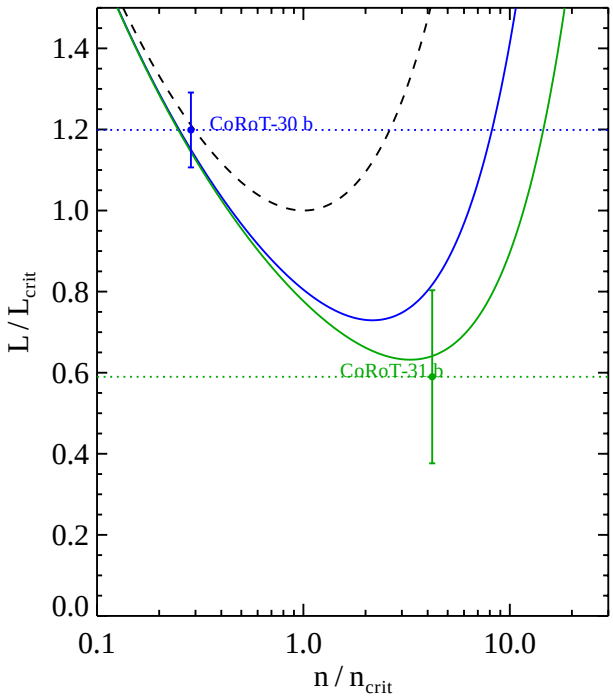

Fig. 14. Darwin diagram for CoRoT-30 b (blue) and CoRoT-31 b (green). The total angular momentum in units of the critical angular momentum is plotted vs. the observed mean motion of the orbit of the planet in units of the critical mean motion. The dashed line is the locus of spin-orbit synchronization. The current positions of the systems are shown with colored dots and corresponding error bars. The tidal evolution would follow the dotted colored line of constant total angular momentum if magnetic braking were negligible. On the other hand, the solid colored lines show the locus of the pseudo-equilibrium, where the angular momentum loss due to the wind is balanced by the angular momentum transferred from the orbit.

majority of known hot Jupiters are Darwin unstable (Damiani & Lanza 2015). This means that tidal evolution will eventually bring the planets increasingly closer to the host until they reach their Roche limits, where the planets will be tidally disrupted. Assuming that angular momentum is conserved, a binary system is Darwin unstable if its total angular momentum $L_{\rm tot}$ is below the critical value $L_{\rm crit}$ (Hut 1980) defined by

$$L_{\rm crit} = 4\left[\frac{G^2}{3^3}\frac{M_\star^3 M_{\rm p}^3}{M_\star + M_{\rm p}}(C_\star + C_{\rm p})\right]^{1/4}, \tag{6}$$

where $C_\star$ and $C_{\rm p}$ are the moments of inertia of the star and the planet, respectively. At $L_{\rm c}$, the unique mean motion corresponding $n_{\rm crit}$ to corotation is

$$n_{\rm crit} = \left(\frac{G^2}{3^3}\frac{M_\star^3 M_{\rm p}^3}{M_\star + M_{\rm p}}\right)^{1/4}(C_\star + C_{\rm p})^{-3/4}. \tag{7}$$

The values of $L_{\rm crit}$ and $n_{\rm crit}$ only depend on the masses and radii of the star and the planet, so that the outcome of tidal evolution of the system can be known for any fully characterized system, even if the details of the tidal dissipation mechanism are not well understood.

However, most observed exoplanet hosts are late-type stars. It is generally admitted that they spin down throughout the main sequence due to magnetic braking. Consequently, the total angular momentum of the star-planet system is not conserved. Moreover, the orbital angular momentum of hot Jupiters is of the same order of magnitude as the rotation angular momentum of their host stars, so that magnetic braking can be important to describe the past and future evolution of orbital elements. As shown by Damiani & Lanza (2015), a state of pseudo-tidal equilibrium is reached when the tidal torque exerted on the star is equal in magnitude and opposite to the wind torque. Binary systems can evolve toward this pseudo-equilibrium when they have $n/n_{\rm crit} \lesssim 0.8$. Using the dimensionless form given in Damiani & Lanza (2015), we can plot in Fig. 14 CoRoT-30 b and CoRoT-31 b in the same Darwin diagram, and determine how they are related to the pseudo-equilibrium state.

To compute the locus of the stellar torque balance, we assumed a Skumanich-type law for magnetic braking calibrated for solar-like stars. We also assumed a tidal dissipation factor $Q'_\star = 10^7$, as expected for this type of star.

It is immediately clear that CoRoT-31 b, like most hot Jupiters, is Darwin unstable. It has currently not enough total angular momentum to evolve toward the synchronization of the orbit and the rotation of the star (black dashed line in Fig. 14). Owing to the mass of the planet, on this close-in orbit, the characteristic timescale for tidal in-spiral is of the order of magnitude of the main-sequence life of the star. This may explain why the planet has survived until the advanced age of the star. Moreover, the current configuration of the system is compatible (within 1σ) or just past the pseudo-equilibrium state, where the tidal torque and the wind torque balance each other (green solid line in Fig. 14). This is expected considering the age of the system; the tides and magnetic braking have had enough time to bring the system to this state of equilibrium and even pass it, regardless of

the initial orbital and rotational configurations at the formation of the planet. The current orbital period of the planet is such that $n/n_{\rm crit} \approx 4.2$, however, so that the pseudo-equilibrium is not stable. The rest of the evolution of the semi-major axis of the planet will be dominated by the tides. In this conditions, CoRoT-31 b will spiral-in towards its Roche limit (corresponding to an orbital period of $P \sim 0.78$ days) with an e-folding time of a few tens of Gyr. However, by this time, the star would have started its giant phase, and the corresponding dramatic increase in radius would certainly lead to the rapid disruption of the planet.

On the other hand, because CoRoT-30 b is at the transition between hot and warm Jupiters, it is Darwin stable within the error bars ($L_{\rm tot}/L_{\rm crit} = 1.2 \pm 0.1$). With $P_{\rm rot}/P_{\rm orb} = 1.18 \pm 0.15$, it is also possible that the orbital period is nearly synchronized with the rotation period within the error bars. However, the continuous loss of angular momentum due to stellar winds prevents the synchronized state from being preserved. Because the tidal torque reaches zero when the orbital period is equal to the rotation period, the magnetic breaking torque currently dominates the tidal torque. Thus the stellar spin slows down faster than the orbit can spin the star up through tides, and because $n/n_{\rm crit} < 0.8$, the system will follow a vertical path in the Darwin diagram until it reaches the balance between tidal torque and breaking torque exerted on the star. Given the current rotation rate of the star, assuming a solar-type braking law and neglecting the spin-up of the star through tidal torque during this phase, this would take about 2 Gyr. The position of CoRoT-30 b in the Darwin diagram is thus consistent with a wind-dominated evolution, currently evolving toward the stationary state, which would be expected for a young system. Thus, although our most likely solution yields a solar-like star well on its main sequence, the combined analysis of the lithium abundances, rotation rate, spectral type of the host, and tidal evolutionary state of the system would tend to favor a younger slightly more massive solution. A better precision on the age of this system would be very useful to constrain migration scenario and gyrochronology relationships. Because this target is very faint, its observation with a sufficient S/N to allow for asteroseismic constrains will be very challenging, even with the space missions TESS and PLATO. Nevertheless, this discussion shows the potential of a full and precise characterization of such a system.

9. Conclusions

Using CoRoT and ground-based follow-up facilities, we discovered two new giant planets at short orbital periods (4.6 and 9.1 days) and measured their radii and masses: 1.01 ± 0.08 $R_{\rm J}$ and 2.90 ± 0.22 $M_{\rm J}$ for CoRoT-30 b, and 1.46 ± 0.30 $R_{\rm J}$ and 0.84 ± 0.34 $M_{\rm J}$ for CoRoT-31 b. In the process, we also characterized their stars: CoRoT-30 and 31 are both solar-like stars, but the former is at the beginning of the main sequence, whereas the latter has just left it. Neither system seems to support the claim that stars hosting planets are more depleted in lithium.

The radii of the two planets are close to the radius of Jupiter, but they differ in mass; CoRoT-30 b is ten times denser than CoRoT-31 b. The core of CoRoT-30 b would weigh between 15 and 75 Earth masses, whereas relatively weak constraints favor no core for CoRoT-31 b. In terms of evolution, the characteristics of CoRoT-31 b appear to be compatible with the high-eccentricity migration scenario; this is not the case for CoRoT-30 b. The angular momentum of CoRoT-31 b is currently too small for the planet to evolve toward synchronization of its orbital revolution with the stellar rotation, and it will slowly spiral-in while its host star becomes a red giant. CoRoT-30 b is not synchronized either: it looses angular momentum owing to stellar winds and is expected to reach steady state in about 2 Gyr. CoRoT-30 and 31, as a pair, are a truly remarkable example of diversity in systems with hot Jupiters.

Acknowledgements. R.F.D. acknowledges the Swiss National Centre for Competence in Research "PlanetS" supported by the Swiss National Science Foundation (SNSF). The German CoRoT team (TLS and University of Cologne) acknowledges DLR grants 50OW0204, 50OW0603, 50OW1403, and 50QM1004. S.C.C.B. acknowledges support from Fundação para a Ciência e a Tecnologia (FCT) through national funds and by FEDER through COMPETE2020 by these grants UID/FIS/04434/2013 & POCI-01-0145-FEDER-007672 and PTDC/FIS-AST/1526/2014 & POCI-01-0145-FEDER-016886; and also acknowledges support from FCT through Investigador FCT contracts IF/01312/2014/CP1215/CT0004. This research has made use of the ExoDat Database, operated at LAM-OAMP, Marseille, France, on behalf of the CoRoT-Exoplanet program, of NASA's Astrophysics Data System, of the Python language with the Matplotlib plotting library and the Scipy scientific computing tools, as well as of Jupyter notebooks for interactive data science and scientific computing. We are grateful to N. Piskunov of Uppsala Astronomical Observatory for making SME available to us, and for answering questions about its implementation and operation.

References

Amard, L., Palacios, A., Charbonnel, C., Gallet, F., & Bouvier, J. 2016, A&A, 587, A105
Auvergne, M., Bodin, P., Boisnard, L., et al. 2009, A&A, 506, 411
Baglin, A., Auvergne, M., Barge, P., et al. 2006, ESA SP, 1306, 33
Bahcall, J. N., & Pinsonneault, M. H. 1992, ApJ, 395, L119
Baranne, A., Queloz, D., Mayor, M., et al. 1996, A&AS, 119, 373
Barnes, S. A. 2007, The ApJ, 669, 1167
Batygin, K., Bodenheimer, P. H., & Laughlin, G. P. 2016, ApJ, 829, 114
Böhm-Vitense, E. 1958, Z. Astrophys., 46, 108
Boisse, I., Bouchy, F., Hébrard, G., et al. 2011, A&A, 528, A4
Boley, A. C., Contreras, A. P. G., & Gladman, B. 2016, ApJ, 817, L17
Bonomo, A. S., Santerne, A., Alonso, R., et al. 2010, A&A, 520, A65
Bordé, P., Fressin, F., Ollivier, M., Léger, A., & Rouan, D. 2007, ASP Conf. Ser., 366, 145
Bordé, P., Bouchy, F., Deleuil, M., et al. 2010, A&A, 520, A66
Bouchy, F., Pepe, F., & Queloz, D. 2001, A&A, 374, 733
Bouvier, J. 2008, A&A, 489, L53
Broeg, C. 2006, PhD Thesis, Friedrich-Schiller-Universität Jena, Germany
Broeg, C. H. 2009, Icarus, 204, 15
Broeg, C. H., & Benz, W. 2012, A&A, 538, A90
Broeg, C., Benz, W., & Wuchterl, G. 2010, Euro. Planet. Sci. Cong., 2010, 623
Bruntt, H., Bedding, T. R., Quirion, P.-O., et al. 2010, MNRAS, 405, 1907
Cardelli, J. A., Clayton, G. C., & Mathis, J. S. 1989, ApJ, 345, 245
Casagrande, L., Ramírez, I., Meléndez, J., & Asplund, M. 2012, ApJ, 761, 16
Chaintreuil, S., Deru, A., Baudin, F., et al. 2016, II.4 The "Ready to Use" CoRoT data, ed. A. Baglin (France: EDP Sciences), 61
Chen, Y. Q., & Zhao, G. 2006, AJ, 131, 1816
Christensen-Dalsgaard, J. 2008, Ap&SS, 316, 13
Creevey, O. L., Thévenin, F., Berio, P., et al. 2015, A&A, 575, A26
Damiani, C., & Lanza, A. F. 2015, A&A, 574, A39
Dawson, R. I., Murray-Clay, R. A., & Johnson, J. A. 2015, ApJ, 798, 66
Deeg, H. J., & Doyle, L. R. 2013, Astrophysics Source Code Library [record ascl:9911.002]
Deeg, H. J., Gillon, M., Shporer, A., et al. 2009, A&A, 506, 343
Deleuil, M., Meunier, J. C., Moutou, C., et al. 2009, AJ, 138, 649
Delgado Mena, E., Israelian, G., González Hernández, J. I., et al. 2014, A&A, 562, A92
Díaz, R. F., Almenara, J. M., Santerne, A., et al. 2014, MNRAS, 441, 983
Eggleton, P. P., Faulkner, J., & Flannery, B. P. 1973, A&A, 23, 325
Etzel, P. B. 1981, Photometric and Spectroscopic Binary Systems, eds. E. B. Carling, & Z. Kopal (Berlin: Springer), 111
Ford, E. B., & Rasio, F. A. 2006, ApJ, 638, L45
Fridlund, M., Hébrard, G., Alonso, R., et al. 2010, A&A, 512, A14
Gandolfi, D., Parviainen, H., Deeg, H. J., et al. 2015, A&A, 576, A11
Gray, R. O., & Corbally, C. J. 1994, AJ, 107, 742
Gregory, P. C. 2005, Bayesian Logical Data Analysis for the Physical Sciences: a Comparative Approach with Mathematica Support (Cambridge: Cambridge University Press)
Grevesse, N., & Noels, A. 1993, in Origin and Evolution of the Elements, eds. N. Prantzos, E. Vangioni-Flam, & M. Casse (Singapore: World Scientific), 15

Grevesse, N., & Sauval, A. J. 1998, Space Sci. Rev., 85, 161
Gustafsson, B., Edvardsson, B., Eriksson, K., et al. 2008, A&A, 486, 951
Han, E., Wang, S. X., Wright, J. T., et al. 2014, PASP, 126, 827
Hauschildt, P. H., Allard, F., & Baron, E. 1999, ApJ, 512, 377
Hut, P. 1980, A&A, 92, 167
Iglesias, C. A., & Rogers, F. J. 1996, ApJ, 464, 943
Israelian, G., Delgado Mena, E., Santos, N. C., et al. 2009, Nature, 462, 189
Ivanov, P. B., & Papaloizou, J. C. B. 2007, MNRAS, 376, 682
Jeffries, R. D. 2014, EAS Pub. Ser., 65, 289
Kass, R. E., & Raftery, A. E. 1995, J. Am. Stat. Assoc., 90, 773
Kurucz, R. 1993, SYNTHE Spectrum Synthesis Programs and Line Data. Kurucz CD-ROM (Cambridge, MA: Smithsonian Astrophysical Observatory), 1993, 18
Kurucz, R. L. 1979, ApJS, 40, 1
Kurucz, R. L. 2013, Astrophysics Source Code Library [record ascl:1303.024]
Lejeune, T., Cuisinier, F., & Buser, R. 1997a, A&AS, 125, 229
Lejeune, T., Cuisinier, F., & Buser, R. 1997b, VizieR Online Data Catalog: J/A+AS/125/229
Lin, D. N. C., Bodenheimer, P., & Richardson, D. C. 1996, Nature, 380, 606
Lind, K., Asplund, M., & Barklem, P. S. 2009, A&A, 503, 541
Mayor, M., Marmier, M., Lovis, C., et al. 2011, ArXiv e-prints [arXiv:1109.2497]
Mayor, M., Pepe, F., Queloz, D., et al. 2003, The Messenger, 114, 20
Meléndez, J., Schuster, W. J., Silva, J. S., et al. 2010, A&A, 522, A98
Michaud, G., & Proffitt, C. R. 1993, ASP Conf. Ser., 40, 246
Nelson, B., & Davis, W. D. 1972, ApJ, 174, 617
Pepe, F., Mayor, M., Galland, F., et al. 2002, A&A, 388, 632
Pietrinferni, A., Cassisi, S., Salaris, M., & Castelli, F. 2004, ApJ, 612, 168
Popper, D. M., & Etzel, P. B. 1981, AJ, 86, 102
Queloz, D., Henry, G. W., Sivan, J. P., et al. 2001, A&A, 379, 279
Ramírez, I., Fish, J. R., Lambert, D. L., & Allende Prieto, C. 2012a, ApJ, 756, 46
Ramírez, I., Michel, R., Sefako, R., et al. 2012b, ApJ, 752, 5
Rasio, F. A., & Ford, E. B. 1996, Science, 274, 954
Santerne, A., Endl, M., Hatzes, A., et al. 2011, Eur. Phys. J. Web Conf., 11, 02001
Santerne, A., Díaz, R. F., Almenara, J.-M., et al. 2015, MNRAS, 451, 2337
Santerne, A., Moutou, C., Tsantaki, M., et al. 2016, A&A, 587, A64
Southworth, J. 2011, MNRAS, 417, 2166
Straizys, V., & Kuriliene, G. 1981, Ap&SS, 80, 353
Valenti, J. A., & Piskunov, N. 1996, A&AS, 118, 595
Valenti, J. A., & Fischer, D. A. 2005, ApJS, 159, 141

[1] Laboratoire d'astrophysique de Bordeaux, Univ. Bordeaux, CNRS, B18N, allée Geoffroy Saint-Hilaire, 33615 Pessac, France
e-mail: pascal.borde@u-bordeaux.fr
[2] Observatoire astronomique de l'Université de Genève, 51 ch. des Maillettes, 1290 Versoix, Switzerland
[3] Universidad de Buenos Aires, Facultad de Ciencias Exactas y Naturales. Buenos Aires, Argentina
[4] CONICET – Universidad de Buenos Aires. Instituto de Astronomía y Física del Espacio (IAFE). Buenos Aires, Argentina
[5] Université Côte d'Azur, Observatoire de la Côte d'Azur, CNRS, Laboratoire Lagrange, Bd de l'Observatoire, CS 34229, 06304 Nice Cedex 4, France
[6] Institut d'astrophysique spatiale, Univ. Paris-Sud, CNRS, 91405 Orsay, France
[7] Max-Planck-Institut für Sonnensystemforschung, Justus-von-Liebig-Weg 3, 37077 Göttingen, Germany
[8] Dipartimento di Fisica, Universitá di Torino, via P. Giuria 1, 10125 Torino, Italy
[9] Landessternwarte Königstuhl, Zentrum für Astronomie der Universität Heidelberg, Königstuhl 12, 69117 Heidelberg, Germany
[10] Instituto de Astrofísica de Canarias, 38205 La Laguna, Tenerife, Spain
[11] Universidad de La Laguna, Dept. de Astrofísica, 38206 La Laguna, Tenerife, Spain
[12] Max-Planck-Institut für Astronomie, Königstuhl 17, 69117 Heidelberg, Germany
[13] Leiden Observatory, University of Leiden, PO Box 9513, 2300 RA Leiden, The Netherlands
[14] Department of Earth and Space Sciences, Chalmers University of Technology, Onsala Space Observatory, 439 92 Onsala, Sweden
[15] Department of Physics, Denys Wilkinson Building, Keble Road, Oxford, OX1 3RH, UK
[16] Aix Marseille Univ, CNRS, LAM, Laboratoire d'Astrophysique de Marseille, Marseille, France
[17] LESIA, Observatoire de Paris, Univ. Pierre & Marie Curie, Univ. Paris-Diderot, CNRS, 5 place J. Janssen, 92195 Meudon, France
[18] Instituto de Astrofísica e Ciências do Espaço, Universidade do Porto, CAUP, Rua das Estrelas, PT4150-762 Porto, Portugal
[19] INAF-Osservatorio Astrofisico di Torino Strada Osservatorio, 20 10025 Pino Torinese (TO), Italy
[20] Institute of Planetary Research, German Aerospace Center, Rutherfordstrasse 2, 12489 Berlin, Germany
[21] IAG-Universidade de São Paulo, 1226 São Paulo, Brasil
[22] Thüringer Landessternwarte, Sternwarte 5, Tautenburg 5, 07778 Tautenburg, Germany
[23] Rheinisches Institut für Umweltforschung an der Universität zu Köln, 50931 Aachener Strasse 209, Germany
[24] Institut d'astrophysique de Paris, Univ. Pierre & Marie Curie, CNRS, 98 bis boulevard Arago, 75014 Paris, France
[25] School of Physics and Astronomy, Raymond and Beverly Sackler Faculty of Exact Sciences, 39040 Tel Aviv University, Tel Aviv, Israel
[26] Sub-department of Astrophysics, Department of Physics, University of Oxford, Oxford, OX1 3RH, UK
[27] Center for Astronomy and Astrophysics, TU Berlin, Hardenbergstr. 36, 10623 Berlin, Germany
[28] LUTH, Observatoire de Paris, Univ. Paris-Diderot, CNRS, 5 place Jules Janssen, 92195 Meudon, France
[29] Kuffner Observatory, Johann-Staud-Straße 10, 1160 Vienna, Austria

Appendix A: Computation of the contamination

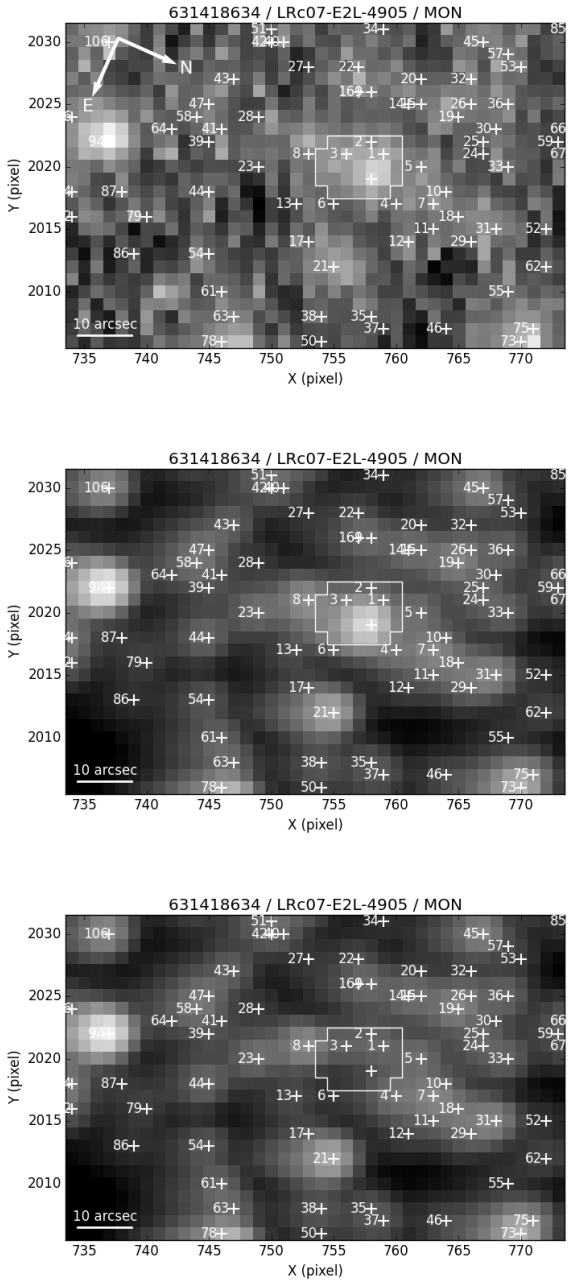

Fig. A.1. CoRoT thumbnails, i.e., target-centered CCD subimages, for CoRoT-30. The photometric mask for the target stars appears in white. The white crosses indicate the locations of the neighboring stars retrieved from Exodat. *Top image*: observed data. *Middle image*: noise-free computed data. *Bottom image*: same as the middle one without the target PSF to clearly show the contamination by neighboring stars. We note the significant contamination for CoRoT-30.

We compute the contamination for CoRoT targets here with noise-free thumbnails, that is, target-centered CCD subimages. This process implies (1) identifying the neighboring stars in Exodat, (2) computing their $V-R$ colors, (3) estimating their effective temperatures from their colors, (4) selecting their point spread functions (PSFs) in the CoRoT PSF database as a function of their effective temperatures and positions on the CCD,

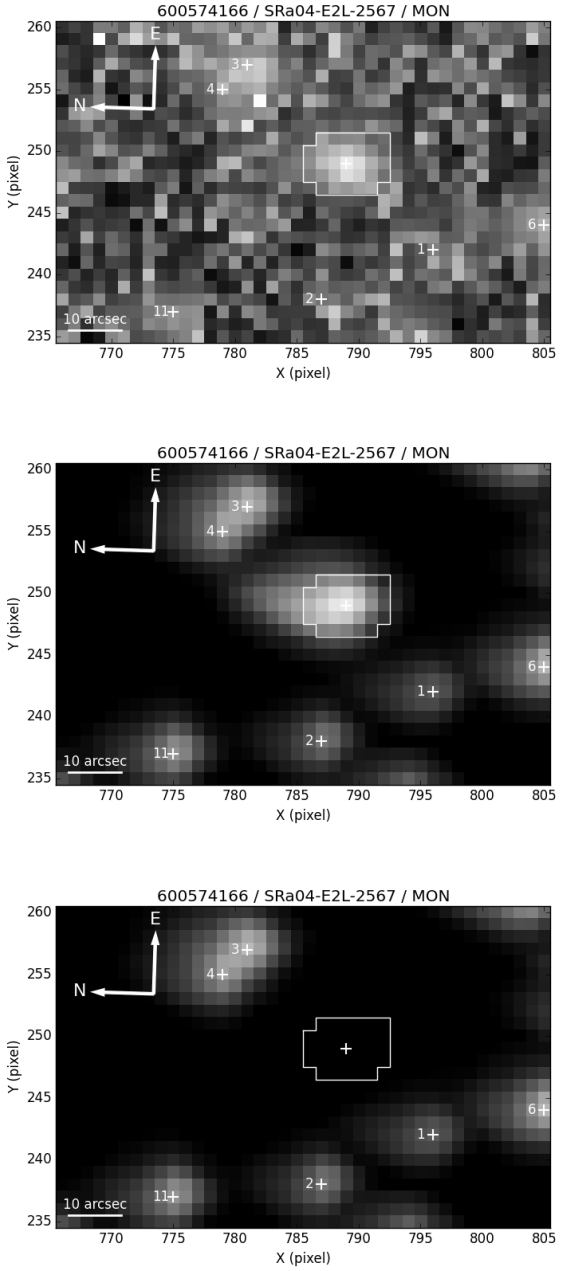

Fig. A.2. CoRoT thumbnails, i.e., target-centered CCD subimages, for CoRoT-31. The photometric mask for the target stars appears in white. The white crosses indicate the locations of the neighboring stars retrieved from Exodat. *Top image*: observed data. *Middle image*: noise-free computed data. *Bottom image*: same as the middle one without the target PSF to clearly show the contamination by neighboring stars. We note the negligible contamination for CoRoT-31.

(5) rescaling their PSF amplitudes using their R magnitudes, (6) repositioning the rescaled PSFs in the computed imagettes, and (7) isolating the neighboring star pixels that land in the target photometric mask. The top and middle images in Figs. A.1 and A.2 show the observed and computed thumbnails for comparison and reconstruction quality control. In the bottom images, the target star PSFs are removed so that the contamination can be computed by reference with the middle images. The contamination is clearly significant for CoRoT-30, but negligible for CoRoT-31.